



THE UNIVERSITY *of* EDINBURGH

Edinburgh Research Explorer

A tale of two (or more) h's

Citation for published version:

Brieden, S, Gil-Marín, H & Verde, L 2023, 'A tale of two (or more) h's', *Journal of Cosmology and Astroparticle Physics (JCAP)*, vol. 2023, no. 4, 023, pp. 1-43. <https://doi.org/10.1088/1475-7516/2023/04/023>

Digital Object Identifier (DOI):

[10.1088/1475-7516/2023/04/023](https://doi.org/10.1088/1475-7516/2023/04/023)

Link:

[Link to publication record in Edinburgh Research Explorer](#)

Document Version:

Peer reviewed version

Published In:

Journal of Cosmology and Astroparticle Physics (JCAP)

General rights

Copyright for the publications made accessible via the Edinburgh Research Explorer is retained by the author(s) and / or other copyright owners and it is a condition of accessing these publications that users recognise and abide by the legal requirements associated with these rights.

Take down policy

The University of Edinburgh has made every reasonable effort to ensure that Edinburgh Research Explorer content complies with UK legislation. If you believe that the public display of this file breaches copyright please contact openaccess@ed.ac.uk providing details, and we will remove access to the work immediately and investigate your claim.



A tale of two (or more) h 's

Samuel Brieden^{1,2} Héctor Gil-Marín² Licia Verde^{2,3}

¹Institute for Astronomy, University of Edinburgh, Blackford Hill, Edinburgh, EH9 3HJ, UK

²ICC, University of Barcelona, IEEC-UB, Martí i Franquès, 1, E-08028 Barcelona, Spain

³ICREA, Pg. Lluís Companys 23, Barcelona, E-08010, Spain

E-mail: samuel.brieden@ed.ac.uk, hectorgil@icc.ub.edu, liciaverde@icc.ub.edu

Abstract. We use the large-scale structure galaxy data (LSS) from the BOSS and eBOSS surveys, in combination with abundances information from Big Bang Nucleosynthesis (BBN), to measure two values of the Hubble expansion rate, $H_0 = 100h$ [km s⁻¹ Mpc⁻¹], each of them based on very different physical processes. One is a (traditional) late-time-background measurement, based on determining the BAO scale and using BBN abundances on baryons for calibrating its absolute size (BAO+BBN). This method anchors H_0 to the (standard) physics of the sound horizon scale at pre-recombination times. The other is a newer, early-time based measurement, associated with the broadband shape of the power spectrum. This second method anchors H_0 to the physics of the matter-radiation equality scale, which also needs BBN information for determining the suppression of baryons in the power spectrum shape (shape+BBN). Within the Λ CDM model, we find very good consistency among these two H_0 's: BAO+BBN (+growth) delivers $H_0 = 67.42^{+0.88}_{-0.94}$ (67.37^{+0.86}_{-0.95}) km s⁻¹ Mpc⁻¹, whereas the shape+BBN (+growth) delivers $H_0 = 70.1^{+2.1}_{-2.1}$ (70.1^{+1.9}_{-2.1}) km s⁻¹ Mpc⁻¹, where ‘growth’ stands for information from the late-time-perturbations captured by the growth of structure parameter. These are the tightest sound-horizon free H_0 constraints from LSS data to date.

As a consequence, to be viable any Λ CDM extension proposed to address the so-called “Hubble tension” needs to modify consistently not only the sound horizon scale physics, but also the matter-radiation equality scale, in such a way that both late- and early-based H_0 's return results mutually consistent and consistent with the high H_0 value recovered by the standard cosmic distance ladder (distance-redshift relation) determinations.

Contents

1	Introduction	1
2	Standard rulers and cosmological distances	4
3	ShapeFit compression and cosmological interpretation	5
3.1	BAO and geometry information - h from the sound horizon scale	6
3.2	Shape information - h from the equality epoch	8
3.3	Geometry vs. shape - a tale of two h 's	10
3.4	Adding the growth information. Yet another h ?	13
4	Results from BOSS and eBOSS data	18
4.1	The data	18
4.2	Piecewise- Λ CDM constraints from geometry and shape	18
4.3	Piecewise Λ CDM constraints from geometry, shape and growth	21
4.4	Beyond Λ CDM: massive neutrinos and dark-radiation.	24
5	Beyond m - a geometrical interpretation of the shape.	26
5.1	Mock analysis setup	27
5.2	Compressed-variables results	28
5.3	Cosmological interpretation of the mock data	29
6	Discussion and conclusions	32
A	The impact of priors on $\Omega_b h^2$ and n_s	35
B	Summary of all cosmological constraints	37

1 Introduction

Over the last two decades cosmology has become a precision science; cosmological observations have consolidated the standard model of cosmology, the Λ cold dark matter (Λ CDM) model: an effective model with only six parameters, now measured with unprecedented precision. In the near future new surveys e.g., [1–6] are expected to provide further improvements. The model's parameters can, and have been, measured with errors of few percent or sometimes sub-percent using different approaches and different observables that rely on different physics. The resounding success of the Λ CDM model rests on the broad agreement of these different measurements.

Over the last decade or so however, this agreement has worsened progressively and significantly for the Hubble expansion rate today, the parameter H_0 , also expressed through the dimensionless Hubble parameter $h \equiv H_0/(100 \text{ km s}^{-1} \text{ Mpc}^{-1})$. The discrepancy is now at the $\sim 5\sigma$ level [7] and deemed a ‘tension’ [8]. Direct, local measurements of H_0 , based on the traditional cosmic distance ladder and relying on type Ia supernovae (SNe) calibrated through Cepheid stars, report a ‘high- H_0 ’ value of $H_0 = 73.0 \pm 1.0 \text{ km/s/Mpc}$ [7]. But indirect measurements of H_0 , based on the interpretation of Cosmic Microwave Background (CMB) anisotropies within the standard Λ CDM model, yield a ‘low- H_0 ’ value:

$H_0 = 67.4 \pm 0.5$ km/s/Mpc [9]. Other techniques have complemented these two type of measurements: e.g, direct measurements of type Ia SNe calibrated using the tip of Red Giant Branch (TRGB) [10], time-delays in strong lensing systems [11], and indirect measurements from large scale structure data (LSS), which rely on the Baryon Acoustic Oscillation (BAO) feature imprinted on late-time dark matter tracers [12–14]. Observations seem to segregate in two ‘camps’ [15]: local, direct measurements, which cluster around the high- H_0 value, and indirect measurements which fall around the low- H_0 value [8]. Local direct measurements are based on the (direct) cosmic distance ladder approach; indirect measurement broadly fall in the inverse cosmic distance ladder approach [16, 17]. As, after almost a decade of checks by the community, experimental systematics seem to be an increasingly unlikely explanation for the tension, a suite of exotic extensions of the Λ CDM model has been investigated to alleviate this tension e.g., [18, 19] and references therein.

No measurement is completely free of assumptions; relevant to this paper is the fact that indirect determinations of H_0 are particularly reliant on the adopted cosmological model. If the H_0 tension represents a shortcoming of the standard model, indicating that the model is in need of an extension, it is of paramount importance to analyze the data, especially those yielding indirect measurements of H_0 , in the most model-agnostic possible way, making the least possible number of assumptions, and spelling them out clearly. Then, suitable combinations of such measurements can be constructed to design *diagnostic tests* of the Λ CDM model or of proposed extensions.

The recently-developed *ShapeFit* compression technique [20] is particularly well-suited to develop such diagnostic tests for the analysis of galaxy spectroscopic surveys data (see [21, 22]). *ShapeFit* compresses the information enclosed in the full power spectrum anisotropic signal in few physical variables per redshift bin, which are essentially model-independent¹. These variables represent the position of the BAO peak along and across the line-of-sight (LOS) in units of the sound horizon scale, the growth rate of structure, and the slope of the smoothed broadband of the power spectrum pivoting at a certain large reference scale. They effectively parameterise changes of different physical features relative to a linear matter power spectrum template, which is why it is also known as ‘fixed-template’ approach. The four physical variables per redshift bin can be later interpreted in the light of a model, as to extract information about the parameters of that model.

This model-agnostic approach is qualitatively different from other approaches –often referred to as ‘direct fit’ or ‘full-modeling’– which infer the parameters of a given model directly from the full power spectrum signal and simultaneously at all available scales and redshifts (e.g., [23–26]). Within the ‘full-modeling’ approach it is not straightforward to unambiguously disentangle the information relative to different physical processes, and thus it is very difficult to run diagnostic tests of Λ CDM, such as whether the late- and early-time signals are consistent. These diagnostic tests, on the other hand, are enabled by the *ShapeFit* approach: as we illustrate in this paper, by playing with the variables considered during the cosmology inference step, one can turn off and on different assumptions of the model, as the different compressed variables represent early- or late-time physical processes within the model, or express background vs. perturbation physics (see also [27]). One possible initial approach to design a diagnostic test, which we attempt here, is to consider a ‘piecewise’ Λ CDM model: for each relevant epoch or physical process we assume that Λ CDM is an effective model, but we do not necessarily force the inferred parameters of the model to be

¹The variables are model-independent, their interpretation however is not.

coherent across epochs or physical signatures.

These consistency checks are of particular relevance when it comes to indirect (or model-dependent) measurements of H_0 . In a similar way as (direct) distance ladder-based H_0 measurements need low- z ‘anchors’, indirect inverse distance ladder-based H_0 determinations need high- z ‘anchors’, whose notion usually relies on a model. The traditional and best calibrated anchor is the size of the sound horizon at radiation drag, which is usually provided by the analysis of CMB data. The robustness of the direct distance ladder approach relies on having several different ‘anchors’ and calibrators; it is thus important to provide several independent and different anchors also for the inverse ladder.

This paper is one attempt in this direction. We consider and compare different ways of measuring the Hubble expansion rate from large-scale structure data, where each approach relies on different assumptions and physical processes that are in-built in the Λ CDM model. One way is closely related to the traditional, BAOofLSS, approach: measurements of the BAO signal imprinted in the distribution of dark-matter tracers (galaxies, quasars and Lyman- α) at different redshifts, which are calibrated with the absolute size of the sound horizon scale at radiation drag r_d . Instead of being given by the analysis of CMB data, the adopted r_d value is obtained by assuming standard early-time physics and big bang nucleosynthesis (BBN) [28] combined with measurements of abundances of light elements [29]. This method, referred to as BAO+BBN, relies on assuming standard physics at pre-recombination times and provides an indirect measurement of H_0 which is independent of CMB anisotropies [30–33].

An alternative route to H_0 from LSS data is to use the matter-radiation equality scale, k_{eq} , for example employing it as a standard ruler (calibrated also at early times), just as done with the sound horizon scale (e.g., [34] and references therein, also [35]). Unlike the sound horizon r_d , this scale imprints a signal at much larger scales (the matter power spectrum turn-around), and this feature also includes the suppression of power on nearby smaller scales, which is related to how fast modes re-enter the horizon just before matter-radiation equality. One drawback of this approach is that this turn-around feature is not well measured in current LSS surveys: partly because of the limitation of the number of large-scale modes available, and partly because at these scales imaging systematics tend to contaminate the signal of the power spectrum significantly. However, information can still be accessed in the broadband shape of the power spectrum at scales just below the turn-around, typically $0.03 < k \text{ [hMpc}^{-1}] < 0.10$ [21, 36–39], which are also sensitive to the physics around matter-radiation equality times. From the *ShapeFit* perspective this information is encoded by the slope of the smoothed broadband of the power spectrum.

Having two distinct measurements of the Hubble parameter, informed by very different physical processes (right before recombination or at matter-radiation equality epochs), is very important to shed light on the current H_0 -tension. Any proposed solution to the Hubble tension should improve the performance of Λ CDM in terms of agreement of all the different H_0 ’s, and also improve, or at least not worsen, other emerging tensions such as the σ_8 tension (see e.g. [40] and references therein).

The main goal of this paper is then twofold:

1. to obtain the tightest constraints on H_0 from LSS spectroscopic data to date which are independent from the sound horizon at radiation drag and based on Λ CDM matter-radiation equality physics,
2. to provide an array of internal consistency checks of the cosmological model, assuming that systematic effects in the observations are under control (alternatively it can provide

an internal consistency test of the observations themselves, but we will not consider this case here). In particular, the goal is to determine whether this measurement is in agreement with that provided by sound-horizon scale BAOofLSS-type of analyses, where the sound horizon ruler is calibrated assuming Λ CDM pre-recombination physics.

These type of checks can then provide diagnostic tests for the Λ CDM model and ‘guardrails’ for new physics beyond Λ CDM.

The rest of the paper is structured as follows. In section 2 we review very pedagogically the assumptions that a ruler must fulfill to be called standard, and which of these conditions will be assumed later when performing the analysis. In section 3 we summarise some notions and dependencies we expect to obtain when we infer constraints on parameters of Λ CDM type of models from the same type of variables as used in *ShapeFit*, and which assumptions are being made when inferring the Hubble expansion rate parameters from different physical variables. Our main results, consisting of the different types of Hubble parameter measurements obtained from the publicly available BOSS and eBOSS compressed physical variables and their physical implications, are presented in section 4. In section 5 we explore in details the differences between the approach of using the matter-radiation equality scale as a standard ruler, and that of using instead the slope of the broadband shape as a feature to infer Hubble parameter measurements. Finally we conclude in section 6.

2 Standard rulers and cosmological distances

Measuring distances in cosmology is one of the most challenging tasks the field routinely faces. Beside standard candles, standard rulers make this possible. In order to convert the observed redshifts and object’s positions in the sky into comoving distances, we can employ the physical size of a certain object or feature (a ruler). The ruler length can be derived from first principles or assumed to be well known. The BAO feature on low redshift clustering of large-scale structure is such a standard ruler, which enables us to employ LSS data to derive geometric constraints on the Universe’s expansion history.

In this work we assume (as it is customary to do but not always spelled out explicitly) that a standard ruler must satisfy the following two key conditions,

- i)* it is isotropic,
- ii)* its length is fixed, it does not evolve with redshift.

A standard ruler is particularly useful if also

- iii)* the length of the ruler is known.

In particular, the sound horizon scale at radiation drag epoch is set by early-time physics and imprints a characteristic scale on the matter clustering early on, which can thus be assumed to be a ruler. This has been key to the spectacular success of BAOofLSS for cosmology. In fact, condition *i)* is very conservative: violating isotropy for rulers set by early-time physics would violate one of the pillars of the Cosmological Principle [41].

For the BAO feature imprinted in late-time dark matter tracers, assumption *ii)* is also very conservative. While there are models predicting a tiny redshift dependence of the feature connected to the sound horizon due to non-linear couplings [42], these effects are usually taken into account in the standard approach either by modifying the fixed template accordingly or

via reconstruction [43–45]. Beyond that, no cosmological models exist (yet) that would predict a running of the BAO scale with redshift. As such a scenario lacks of physical motivation, assumption *ii*) is usually considered true, such that the sound horizon can indeed be treated as a standard ruler.

Condition *iii*), however, requires that the BAO scale, as seen in the late-time clustering, can be uniquely identified with the sound horizon (i.e., no mismatch) and requires a model of the early Universe (although not necessarily early Universe data). Although such a mismatch between the physical sound horizon inferred from the CMB and the length of the standard ruler observed in the BAO has been quantified already following perturbation theory arguments [46–48], this shift is small enough not to be statistically relevant (yet) and could easily be incorporated in the modeling. Then, for a Λ CDM model for example, it can be set by late-Universe observations of baryon abundances when the physics of specific early-Universe epochs is assumed to be known.

In the case of standard candles, the magnitude of supernovae can be known to be fixed only under certain conditions or assumptions. For this reason sometimes supernovae Ia are called “standardizable” candles. Similarly, the length of a standard ruler could be known, or known to be fixed, only under certain assumptions. One could then also use the word “standardizable” rulers. Here we spell out clearly the assumptions under which a given ruler can be considered standard. Along this paper we will comment on which of the above 3 assumptions about the properties of a ruler are used when deriving constraints on the Hubble parameter.

3 ShapeFit compression and cosmological interpretation

This work makes use of the *ShapeFit* methodology introduced in [20], which has passed blind high precision validation tests on the large volume of the PT challenge simulation [49, 50] in [51]. Recently in [21], *ShapeFit* has been applied to the full BOSS+eBOSS Luminous Red Galaxy (LRG) and Quasar (QSO) samples [52–54], yielding constraints on cosmological parameters with unprecedented precision from LSS data alone.

Compared to classic analysis approaches relying on the BAO and redshift space distortion (RSD) signals, the additional constraining power of *ShapeFit* mainly comes from the large-scale shape of the linear matter power spectrum, $k < 0.1 h \text{ Mpc}^{-1}$, encapsulated by a new degree of freedom of the template-fit, the shape parameter m [55]. This has been subsequently corroborated by [56, 57] who showed that even for direct model fits which include smaller scales pushing into the non-linear regime, most of the robust cosmological signal is encoded in the large scales.

Here we build on these findings by providing a modular cosmological analysis of each of the physical features captured by *ShapeFit* and focusing on their individual relation with the Hubble parameter. For that, we use the measured compressed variables $\Theta(z)$ of BOSS DR12 LRG (the first two overlapping redshift bins, $0.2 < z < 0.5$ and $0.4 < z < 0.6$), eBOSS DR16 LRG ($0.6 < z < 1.0$) and eBOSS DR16 QSO ($0.8 < z < 2.2$) samples provided in appendix E of [21],

$$\Theta(z) = \{D_H(z)/r_d, D_M(z)/r_d, f(z)\sigma_{s8}(z), m(z)\}, \quad (3.1)$$

where $D_H(z)$ and $D_M(z)$ represent the distance along and across the LOS, respectively, r_d is the sound horizon scale at baryon drag used as standard ruler in the fixed-template method, $f(z)$ is the logarithmic growth rate of structure, $\sigma_{s8}(z)$ is the linear matter fluctuation

amplitude filtered on the scale of $8 r_{\text{d}}^{\text{fid}} r_{\text{d}}^{-1} h^{-1} \text{Mpc}$, and $m(z)$ (or the shape parameter) is the linear power spectrum slope at a pivot scale of $k_p = \pi/r_{\text{d}}$.

We now summarize the physical signal each of these quantities encode, focusing on their cosmological implications and in particular how they can be used to obtain qualitatively different measurements of h . Subsections 3.1, 3.2 and 3.3 are somewhat pedagogical, but provide key concepts to highlight the motivation of this work.

3.1 BAO and geometry information - h from the sound horizon scale

The first two quantities, $D_H(z)/r_{\text{d}}$ and $D_M(z)/r_{\text{d}}$, contain purely geometrical information. The numerators, $D_H(z)$ and $D_M(z)$ are determined by the late-time (post-recombination) geometry, setting the *coordinate* system of the universe. The denominator, the sound horizon scale r_{d} , is set by early-time (pre-recombination) physics; by design it is a standard ruler and yields the natural *unit* system for the BAO-based geometric probe. By construction, fixed-template fits such as the standard BAO, RSD and *ShapeFit* analyses yield distance measurements *in units of the standard ruler* which are independent of the adopted template. In such analyses the ruler length is unknown *a priori* and its absolute value can only be inferred (indirectly) under the assumption of a model of the early-universe.

Now, it is interesting to take a closer look at the very different cosmological implications of the early- and late-time quantities separately, in particular how these relate to the standard ruler assumptions *i) - iii)* (see section 2). For this purpose, it is useful to consider the derived basis, where the signal is explicitly decomposed in an isotropic component and the classic Alcock-Paczynski (AP) parameter, $\{D_V(z)/r_{\text{d}}, F_{\text{AP}}(z)\}$, respectively, defined as,

$$D_V(z)/r_{\text{d}} \equiv \left[z (D_H(z)/r_{\text{d}}) (D_M(z)/r_{\text{d}})^2 \right]^{1/3} = \left[z D_H(z) D_M^2(z) \right]^{1/3} / r_{\text{d}}, \quad (3.2)$$

$$F_{\text{AP}}(z) \equiv \frac{D_M(z)/r_{\text{d}}}{D_H(z)/r_{\text{d}}} = D_M(z)/D_H(z), \quad (3.3)$$

which makes it easier to disentangle the early- and late-time effects. The spherically-averaged distance scaling, $D_V(z)/r_{\text{d}}$, represents the scaling of the late-time isotropic distance $D_V(z)$ versus the early-time sound horizon r_{d} (assumed isotropic in *i)*).

The AP parameter, $F_{\text{AP}}(z)$, is a pure late-time variable which captures the apparent distortion of an isotropic feature (here r_{d} , but any scale can be used as a reference) along vs. across the LOS. Note that for $F_{\text{AP}}(z)$ the only early-time assumption entering this quantity is standard ruler condition *i)*, not *ii)*: eq. (3.3) remains true even if the ruler (the sound horizon) were to change with redshift.

It is possible to separate early- from late-time information in the interpretation of the compressed variables as follows. The redshift dependence of $D_V(z)/r_{\text{d}}$, regardless of the signal amplitude, only encloses information about late-time kinematics. In this case one only uses the relative $D_V(z)/r_{\text{d}}$ information across different redshifts; we refer to this as uncalibrated (do not use of the absolute value of r_{d}) and unnormalized (the overall amplitude of D_V is irrelevant) isotropic distance, which we note as ‘ $\mathfrak{D}_V(z)$ ’.

The AP distortion information (fully described by F_{AP}) combined with the isotropic late-time part, ‘ $\mathfrak{D}_V + F_{\text{AP}}$ ’, represents the full ‘unnormalized and uncalibrated BAO’ information. This information is particularly relevant for model building, since it is associated to the cosmological background only. In fact, its measurement only relies on the assumption of the cosmological principle (e.g., that the universe is homogeneous and isotropic at any given time,

without the need of assuming General Relativity (GR)² and without early-time assumptions (apart from the existence of a standard ruler) and can hence be compared to the uncalibrated SNe Pantheon Ω_m measurement. For a Friedmann-Lemaître-Robertson-Walker universe (and for any theory of gravity) in combination with SNe, BAOofLSS can be used to constrain the Etherington relation and global curvature. It is well known that the AP test, within the flat Λ CDM model (at late-time), constrains Ω_m ; within a more general dark energy model it can also constrain its associated equation of state parameter(s).

There is also an intermediate step, whereby the absolute value of D_V (i.e., normalized) but uncalibrated ruler (so condition *iii*) still does not apply), D_V/r_d , is considered. This is what gives the usual combination hr_d that standard BAOofLSS analyses retrieve. Then, the final step is to get a value or constraint on r_d (i.e., now *iii*) does apply) to finally obtain h [58–60]. Hence, the BAOofLSS information alone (in terms of angles and redshifts) is not capable of constraining h unless a certain model is assumed about the early-time physics. Recall that the sound horizon scale is given by,³

$$r_d = \int_{\infty}^{z_d} \frac{c_s(z)}{H(z)} dz \simeq |_{\Lambda\text{CDM}} \frac{147.05}{\text{Mpc}} \left(\frac{\Omega_m h^2}{0.1432} \right)^{-0.23} \left(\frac{N_{\text{eff}}}{3.04} \right)^{-0.1} \left(\frac{\Omega_b h^2}{0.02236} \right)^{-0.13}, \quad (3.4)$$

where z_d denotes the redshift at radiation drag, and c_s is the sound speed in the photon-baryon fluid (and we have used eq. 2.4 of [33] on the RHS). For example, within a flat Λ CDM model (shortly) before recombination, with fixed CMB temperature, r_d is a function of the physical matter density $\omega_m \equiv \Omega_m h^2$ and the physical baryon density $\omega_b \equiv \Omega_b h^2$ only. Note that for more exotic models, such as those with dark radiation or with early dark energy, this is no longer the case. But for standard early-time physics, the BAO measurement of hr_d and Ω_m can be assisted by a BBN prior on $\Omega_b h^2$ to provide a measurement of h . Invoking such a prior on the physical baryon density is the methodology chosen in this paper, as further specified in section 4.1. For a more sophisticated treatment we refer to [33], where *ShapeFit* is combined with the full BBN likelihood operating with the exact measurements of the relevant nuclear reaction rates. All the results obtained from BOSS+eBOSS for the respective cases mentioned here are shown in section 4.

As noted before, exotic dark-radiation models aim to explain the Hubble tension as an effect of a dark-radiation component on the expansion rate at pre-recombination times, which modifies the sound horizon scale. As noted by [62], an increased expansion rate at early-times leads to a decrease of r_d , essentially because the time required to reach the threshold temperature for decoupling is lower. However, this prior-to-recombination change in the shape of $H(z)$ may also impact other relevant scales such as the sound horizon at matter-radiation equality and the scale of photon diffusion at recombination. Current LSS and CMB data yield tight constraints on these scales, therefore naive dark-radiation models which aim to solve the Hubble tension may fail to provide a good description of other observables.

To understand how internal tensions in the LSS data might hint to new physics beyond the standard, vanilla, Λ CDM model, we consider the isotropic BAO distances given by the

²A small caveat is due: in practice the BAO compressed variables are often extracted from the data after the so-called reconstruction step. Reconstruction is designed to undo the linear bulk-flows and non-linear peculiar motion, reduce statistical and systematic errors associated with non-linearities and hence sharpen the BAO signal. Reconstruction assumes a model for the growth of structure and thus GR. However these are small corrections and apply to small enough scales where Newtonian gravity holds and GR effects are unimportant.) see e.g., [45] and references therein.

³Alternative scaling reported by [61] is $r_d \simeq \frac{55.154e^{-72.3(w_\nu+0.0006)^2}}{(w_c+w_b)^{0.25351}w_b^{0.12807}}$, which we report here just for reference.

Planck best-fit cosmology under the assumption of a Λ CDM model at different redshifts of interest:

$$D_V(z = 0.38) \simeq_{|\Lambda\text{CDM}} \frac{1477.07}{[\text{Mpc}]} \left(\frac{\Omega_m}{0.316} \right)^{-0.11} \left(\frac{h}{0.674} \right)^{-1}; \quad (3.5)$$

$$D_V(z = 0.70) \simeq_{|\Lambda\text{CDM}} \frac{2375.74}{[\text{Mpc}]} \left(\frac{\Omega_m}{0.316} \right)^{-0.18} \left(\frac{h}{0.674} \right)^{-1}; \quad (3.6)$$

$$D_V(z = 1.48) \simeq_{|\Lambda\text{CDM}} \frac{3808.19}{[\text{Mpc}]} \left(\frac{\Omega_m}{0.316} \right)^{-0.29} \left(\frac{h}{0.674} \right)^{-1}; \quad (3.7)$$

$$D_V(z = 2.44) \simeq_{|\Lambda\text{CDM}} \frac{4603.25}{[\text{Mpc}]} \left(\frac{\Omega_m}{0.316} \right)^{-0.34} \left(\frac{h}{0.674} \right)^{-1}. \quad (3.8)$$

Considering now the sound horizon dependence within the early-time physics given by Λ CDM with fixed number of neutrino species and fixed baryon density we can write the above expressions as,

$$\frac{D_V(z = 0.38)}{r_d} \simeq_{|\Lambda\text{CDM}} 10.04 \left(\frac{\Omega_m}{0.316} \right)^{0.12} \left(\frac{h}{0.674} \right)^{-0.54}; \quad (3.9)$$

$$\frac{D_V(z = 0.70)}{r_d} \simeq_{|\Lambda\text{CDM}} 16.15 \left(\frac{\Omega_m}{0.316} \right)^{0.047} \left(\frac{h}{0.674} \right)^{-0.54}; \quad (3.10)$$

$$\frac{D_V(z = 1.48)}{r_d} \simeq_{|\Lambda\text{CDM}} 25.90 \left(\frac{\Omega_m}{0.316} \right)^{-0.058} \left(\frac{h}{0.674} \right)^{-0.54}; \quad (3.11)$$

$$\frac{D_V(z = 2.4)}{r_d} \simeq_{|\Lambda\text{CDM}} 31.30 \left(\frac{\Omega_m}{0.316} \right)^{-0.11} \left(\frac{h}{0.674} \right)^{-0.54}. \quad (3.12)$$

These scalings are illustrated and discussed below, in figure 1. Note that measurements of the unnormalized and uncalibrated D_V/r_d at different redshifts, $\mathfrak{D}_V(z)$, yield a constraint on Ω_m , whereas the normalized (but uncalibrated) $D_V(z)/r_d$ measurements additionally yield a constraint on hr_d , both solely based on late-time physics and late-time observables.⁴

3.2 Shape information - h from the equality epoch

The main new ingredient of *ShapeFit*, the compressed variable capturing the shape, $m(z)$, is obtained from the data in a model-independent way and its measurement can be compared to any cosmological model of choice in a later step.

There is a variety of physical effects that modify the power spectrum shape in a trivial or non-trivial way. These include: the scale-independent scalar tilt n_s of the primordial power spectrum, scale-dependent shape variations due to the scale of equality between matter and radiation, the baryon suppression or the free-streaming scale of massive neutrinos. While all of these effects have very different signatures on the matter power spectrum when considering the full wave-vector range in principle accessible by observations, their behaviour is qualitatively similar in the range of interest for galaxy clustering, $0.02 < k [h\text{Mpc}^{-1}] < 0.20$, (see for example figures 1 and 4 of [20]). This justifies the interpretation of the measurement of the effective parameter $m(z)$ within any model that does not involve severe scale-dependent changes in slope. Still, it is important to note that the shape is *not* a pure late-time or

⁴While the measurements are based on late-time quantities and physics, r_d is an early-time quantity sensitive to early-time physics.

early-time parameter, but rather captures several physical effects ranging from the epoch of inflation until today [55].

Nevertheless, under certain assumptions, the shape can be used to obtain a (model-dependent) constraint of h . First of all we need to assume that the measured large-scale clustering (at $k < 0.1 \text{ hMpc}^{-1}$) reflects faithfully the shape of the matter transfer function (e.g., the galaxy bias is scale-independent at these large, linear scales). Second, a prior on the scalar tilt n_s , which under the inflation-motivated assumption of a power-law primordial power spectrum is very well measured by CMB data [9, 63, 64] due to the wide range of scales covered, needs to be imposed. This prior is needed given that, for the current data sensitivity, the degeneracy between the scale-independent (n) and scale dependent (m) slopes introduced in [20] cannot be effectively broken within *ShapeFit*, although this may change with future surveys probing larger volumes. Third, a prior on the baryon density, $\Omega_b h^2$, is needed, because this parameter controls the baryon suppression in the matter transfer function, which is degenerate with m . This can be obtained either from CMB observations or adopting a BBN-motivated prior as discussed in section 3.1. Finally, the presence of massive neutrinos leads to a signature in the linear power spectrum which is degenerate with m ; we study this in more detail in section 4.3.

To summarize, by assuming fixed fiducial values for, or imposing priors on, n_s , $\Omega_b h^2$ and the sum of neutrino masses Σm_ν (or giving it some upper limit), we effectively calibrate the shape variable, $m(z)$. This is the model-dependent, but necessary step, before making m a variable that captures the signature of early-time physical processes. With this, this variable can be related directly to how fast modes re-enter the horizon at the end of the radiation dominated era, where their logarithmic growth is gradually suppressed along with the increasing importance of the matter density relative to radiation. This is the physical signature that the large-scale shape of the matter transfer function captures: the evolution of the growth suppression of the last few modes that enter the horizon just before matter domination. In this sense the calibrated m is a *speedometer* of how fast the horizon was expanding at that epoch, and this is the physical signature that will be used to measure the Hubble expansion rate. In particular, if the Universe is effectively Λ CDM at times around matter-radiation equality, k_{eq} is set by the parameter combination $\Omega_m h^2|_{\text{eq}}$. Here we have explicitly indicated that this early-time quantity is set by matter-radiation equality physics. With the above caveats and assumptions, indeed we find that the relation between m and k_{eq} is well approximated by,

$$\frac{k_{\text{eq}}}{k_{\text{eq}}^{\text{fid}}} = 0.77m^4 + 0.80m^3 + 0.96m^2 + 1.16m + 1. \quad (3.13)$$

Note that the equality scale can be used as a standard ruler [34], with its own scaling parameters F_{AP} and $D_V(z)k_{\text{eq}}$, yielding a self-contained constraint on Ω_m (for uncalibrated and unnormalized geometric measurements) and on h for the calibrated and normalized quantities, in the exact way as being done for the sound horizon scale. Such a measurement has not been done yet on real data, although this would be close to the parameterisation chosen by [65] for Lyman- α analyses beyond the BAO. We investigate the prospect of such an equality based standard ruler approach in section 5. Instead, the m -based analysis does not employ this scale as a standard ruler, but gives an indirect determination of this early-time quantity through its feature on the matter power spectrum (the shape once calibrated on n_s , $\Omega_b h^2$ and Σm_ν) rather than its position in scale.

As previously mentioned, the shape is directly coupled to the scale of equality in coordinates $m \propto k_{\text{eq}} [\text{Mpc}^{-1}] \propto \Omega_m h^2$. While under a change of coordinate system towards $h\text{Mpc}^{-1}$ the equality scale obviously transforms as $k_{\text{eq}} [h\text{Mpc}^{-1}] \propto \Omega_m h$, the scaling of the unit-less *shape* variable m with $\Omega_m h^2$ is invariant under such a coordinate transformation: for a given power spectrum, any multiplicative coordinate transformation only changes the horizontal and vertical position in $\log(k) - \log(P(k))$ space while leaving the *shape* intact.

This is the reason why our ‘indirect’ m -based equality measurement is sensitive to the parameter $\Omega_m h^2$.⁵ On the other hand, a ‘direct’ equality measurement based on the standard ruler method (converting angles and redshifts into distances and using the equality scale as a unit) would depend on $\Omega_m h$. This is further explained and explored in section 5.

To summarize, in a Λ CDM model the measurement of m can be interpreted as a constraint on $\Omega_m h^2$, which, in conjunction with the Ω_m constraint from the geometrical, “unnormalized and uncalibrated BAO” information, results in a constraint on h . This constraint is hence independent of the absolute value of the sound horizon, but still (because of the adopted Ω_m constraint) makes use of the fact that the sound horizon is a standard ruler⁶. The same reasoning applies to recent full-modeling approaches for sound horizon-free determinations of the Hubble constant [36–39].

3.3 Geometry vs. shape - a tale of two h ’s

Given the observables related to geometry and growth that *ShapeFit* provides, in this section we would like to explore their cosmological implications and their role in providing an internal consistency check of the underlying model.

In a Planck-calibrated Λ CDM model, the expected relation between Ω_m and h given by a fixed D_V/r_d (calibrated) is shown in the left panel of figure 1 for few representative redshifts, $z = 0.38, 0.70, 1.48, 2.33$ (in solid cyan lines), following the expressions given by eqs. (3.9)-(3.12). The lines intersect at the Planck-calibrated ‘true’ value for Ω_m and h . Similarly, the expected Planck-calibrated relation for m is shown as magenta solid line, which also intersects the D_V/r_d lines at the same point. If the measured value of D_V/r_d were to differ from the Planck Λ CDM prediction by 1% then the cyan lines would shift as indicated by the respective fainter and thinner cyan lines. If the measured value of m were to be different by 0.07 (or a change of 7% in $m+1$) from the expected value, the magenta line would shift as indicated by the fainter and thinner magenta lines. The Ω_m value for the Planck-calibrated model is shown by the grey horizontal line, with a $\pm 5\%$ change also shown. The shaded regions in the right panel of figure 1 represent the constraints from BOSS+eBOSS samples (combination of all the redshift bins) [21] for m (in magenta) and for D_V/r_d (in cyan) for $z = 0.38$ and $z = 0.70$ at 1σ (other redshifts are not shown for visibility purposes), the horizontal grey region represents the Ω_m constraint from the Pantheon+ sample [66, 67]. Also note that when considering D_V/r_d (cyan lines/bands), if we were marginalizing over the absolute size of the sound horizon scale, r_d (\mathfrak{D}_V case), the cyan lines/bands would move, freely but coherently, horizontally in figure 1; h would be totally unconstrained as the system would be uncalibrated). Still, the constraints for the different redshift bins would cross at the same Ω_m value, constraining thus Ω_m as anticipated.

⁵Note that in the discussion in our previous work [55] m was presented to be proportional to $\Omega_m h$. This is incorrect. While the large-scale structure measurement of k_{eq} as a standard ruler does scale $\propto \Omega_m h$, m itself scales $\propto \Omega_m h^2$.

⁶In principle an Ω_m constraint could be obtained from other standards such as the standard ruler explored in section 5 or non-standard-ruler probes such as supernovae. Here we prefer to derive all the constraints as

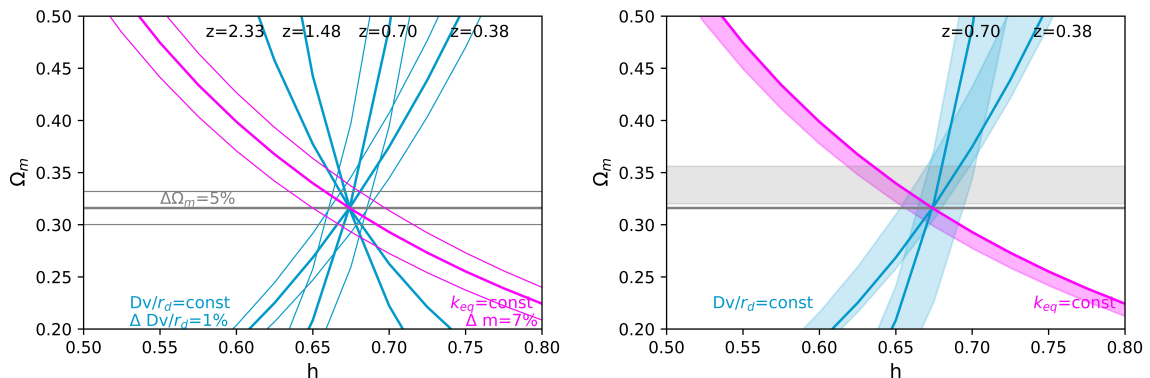


Figure 1. Left panel:

Expected $\Omega_m - h$ plane relations within a Λ CDM model: thick cyan lines show the relation imposed by D_V/r_d predicted by the Planck-calibrated Λ CDM model at representative redshifts (see eqs. (3.9)-(3.12)), the thick magenta line is m (or k_{eq}) constant line which corresponds to a constant $\Omega_m h^2$, also predicted by the Planck-calibrated Λ CDM model; the thick grey line indicates the Ω_m best-fit Planck value. The thinner lines represent shifts from that model as annotated. In particular a 7% shift in $m + 1$ corresponds to a $\sim 9\%$ shift in k_{eq} . Right panel: same, but with semi-transparent colour bands representing selected measurements (1σ confidence levels) from the literature as detailed in the text. The fact that the measured values agree with the expectations offer a powerful consistency check of the model.

From eq. (3.13) it follows that, if k_{eq} were to be 1, 2, or 5% different from the fiducial value assumed, m would change by $\pm(8.5 \times 10^{-3}, 1.7 \times 10^{-2}, 4.3 \times 10^{-2})$, respectively. A change of 7% in $m + 1$ as reported in figure 1 would correspond to a change of about 9% in k_{eq} and thus, a 9% change in $\Omega_m h^2$. In fact, within a Λ CDM model k_{eq} is related to $\Omega_m h^2$ (and hence to m through eq. (3.13)) as,

$$k_{\text{eq}} [\text{Mpc}^{-1}] \simeq_{\Lambda\text{CDM}} 0.010398 \frac{\Omega_m h^2}{0.1432} \left(\frac{2.379 \times 10^4}{\Omega_{\text{rad}} h^2} \right)^{1/2}, \quad (3.14)$$

where Ω_{rad} is the radiation density. The fact that the measured h and Ω_m parameter combinations agree with the Λ CDM prediction is already a powerful consistency check for the model, as figure 1 illustrates. On the other hand, given the measured values for D_V/r_d , F_{AP} and m , we can ask ourselves what can be inferred about the model.⁷

In order to tie together all these quantities, specific aspects of a model have to be assumed at different interpretation stages; a late-time Λ CDM-type expansion history, standard expansion rate around matter-radiation equality, or standard early-type components, such as the sound horizon scale predicted by an early-time Λ CDM model (just) before recombination. But what if one or more of the adopted aspects of the model were incorrect? In this case, when fitting the data, the various parameters, in particular Ω_m and h , would have to be seen as effective parameters: they would be biased, because of the specific shortcomings of the adopted model.

much as possible internally to large-scale structure data currently available.

⁷As explained in section 3.1, F_{AP} also provides a measurement of Ω_m , but we leave it out of our discussion in this section for simplicity.

For example, let us assume some new physics at early time such that the true underlying r_d were to be significantly different (5 or 7%) from the Planck-calibrated Λ CDM value, but the matter density Ω_m was unchanged. If one were to interpret the D_V/r_d constraints within a Λ CDM model, the recovered values of Ω_m and h would move along the $D_V/r_d = \text{constant}$ degeneracy line to compensate: they would be biased. This bias would be different for different redshifts as illustrated in the left panel of figure 2. These shifts may not be observable: the combination of BAO measurements at different redshifts will still yield the (correct) late-time Ω_m value and a biased h value. Hence a direct (local) measurement of h at late-time would signal an issue [68]. The new physics at early times postulated in this example, however, would have to leave k_{eq} (almost) unchanged, given the m constraints. For example, additional dark radiation would change r_d and would bring the early-Universe inferred h value in closer agreement with the local determinations [69]. However enough additional dark radiation to yield a $\sim 7\%$ change in h , would also likely change k_{eq} and BBN: [33] shows that for dark radiation models constraints broaden, but large systematic shifts are disfavoured. Early dark energy models that solve the Hubble tension leave BBN unchanged, modify the expansion rate at matter-radiation equality, but fade away quickly after recombination: this affects therefore r_d , but also k_{eq} .

This argument is parallel to that of [62], but now can be made only referring to late-time observations and independently of the CMB constraints (see also [39]). Of course the m constraints can be ‘evaded’ by allowing the primordial power spectrum spectral slope n_s to deviate from the canonical $n_s \sim 0.96$ values and/or allowing the $\Omega_b h^2$ constraint to deviate from BBN. On the other hand recall that, without assuming an early-time value on r_d , the late-time observations constrain the late-time Ω_m and the combination hr_d , which is an early-time quantity, sensitive to early-time physics.

The right panel of figure 2 illustrates this last point. The cyan lines correspond to constant hr_d values and the magenta lines to constant k_{eq} both under the assumption of a model consistent with Λ CDM at early times (with fixed baryon density), but not necessarily with the same values of cosmological parameters as the late time. In other words the h and Ω_m represented in the right panel of figure 2 are early-time quantities.

To summarize, measurements of the compressed variables of eq. (3.1) can be used to provide a constraint on the late-time matter density parameter, Ω_m^{late} , assuming only isotropy (i.e., condition *i*), through relative measurements of $D_M(z_i)/D_H(z_i)$ at the same redshift) and that the late-time expansion history is that of a flat Λ CDM model. A more stringent constraint can be obtained on Ω_m^{late} if also assuming that the ruler does not evolve with time (i.e., condition *ii*), through relative measurements of $D_V(z_i)/D_V(z_j)$ at the different redshifts), what we refer as the ‘uncalibrated-and-unnormalized’ BAO. Additionally, the normalized-but-uncalibrated BAO yields a measurement of the combination hr_d , sensitive to recombination-time physics. From this a h measurement can be obtained given the knowledge of r_d (condition *iii*), through an early-time physics assumptions, for e.g., eq. (3.4)). For standard early-time physics (during the decade of expansion just before recombination and a baryon density prior [62]), the hr_d constraint yields a degeneracy in the $h^{\text{early},r} - \Omega_m^{\text{early},r}$ plane.⁸ If $\Omega_m^{\text{early}} = \Omega_m^{\text{late}}$, then r_d can be constrained from late-time observations only. This procedure yields the sound-horizon based Hubble parameter, h_{r_d} .

Under the assumption of a Λ CDM-like model at early times, an anchored shape parameter (anchored by a prior on n_s and $\Omega_b h^2$) estimated from galaxy clustering yields constraints

⁸The superscript r explicitly denotes the quantity’s sensitivity to the physics of the recombination epoch.

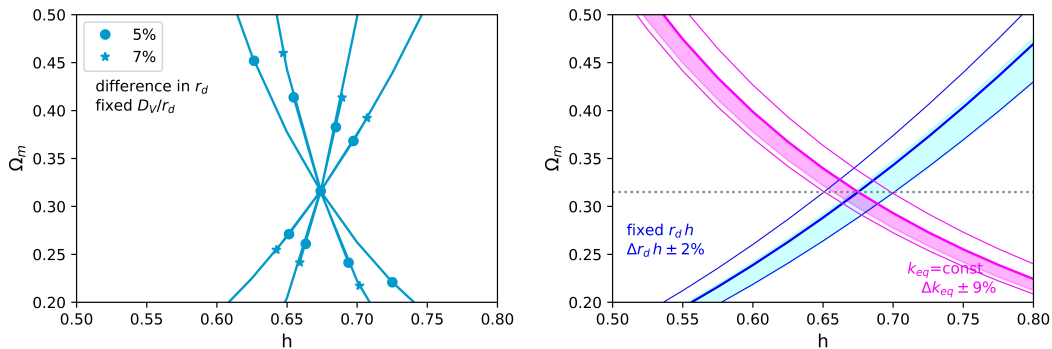


Figure 2. Expected $\Omega_m - h$ plane relations under the assumption of a Λ CDM model. On the left panel: the cyan lines are the same as in the left panel of

figure 1, now indicating how a change in the r_d value (because of new physics in the early universe) would reflect on the Ω_m and h values to keep the BAO-measured quantity D_V/r_d fixed when both r_d and D_V are interpreted in a standard Λ CDM model. This exemplifies how the combination of D_V/r_d measurements at different redshift yield the correct late-time Ω_m even in the case that unknown (or incorrect) early-time physics bias r_d . On the right panel: expected $\Omega_m - h$ plane relations for constant hr_d (cyan) and constant k_{eq} (hence $\Omega_m h^2$, magenta). Despite being constrained by late-time observables, these actually depend on purely early-time quantities. Thinner lines show 2 and 9% (respective) departures from the Λ CDM expected values. The semi-transparent cyan band represents the measured constraints on hr_d obtained by [70] assuming a model-agnostic 4 knots (6 parameters) reconstruction of the late-time expansion history and marginalizing over curvature. The magenta semi-transparent band corresponds to the m constraint from BOSS+eBOSS also shown in the right panel of fig. 1. The horizontal dotted grey line at the fiducial Ω_m value serves to guide the eye; it shows that in a Λ CDM model a 2% change in hr_d should be compensated by a 9% change in k_{eq} to keep Ω_m unchanged.

on $\Omega_m^{\text{early,eq}}(h^{\text{early,eq}})^2$, where we have specified that these are quantities sensitive to physics at equality times (and BBN) rather than at around recombination times. These constraints do not rely on any assumptions about the late-time expansion history, but assume standard early-time physics at the time of the matter-radiation transition, and that late-time processes do not alter the large-linear scales. This degeneracy in the $h - \Omega_m$ plane is different from the one given by D_V/r_d . Thus, another Hubble parameter arises, h_m , when combining this measurement with the Ω_m^{late} determination from geometry, again assuming it is an estimate for Ω_m^{early} ($\Omega_m^{\text{early,eq}}$ in this case).

Moreover, the two degeneracies in the $h - \Omega_m$ plane yield a joint constraint i.e., $h_{(m,r_d)}$ and Ω_m (assuming $\Omega_m^{\text{early,r}} = \Omega_m^{\text{early,eq}}$), the latter can be compared with the geometric determination of Ω_m^{late} . These three h are not statistically independent, as to obtain h_{r_d} and h_m we have used the same Ω_m^{late} geometric determination. In section 4.2 we extract all these quantities from state of the art data.

3.4 Adding the growth information. Yet another h ?

The redshift space distortion signal is efficiently captured by the compressed variable $f\sigma_{88}$, which is readily interpreted as the growth rate $f \equiv d \ln D / d \ln a$, where $D(z)$ is the linear growth factor of perturbations, combined with the rms amplitude of matter fluctuations,

which is closely related to the σ_8 cosmological parameter. The extraction of this compressed variable relies on relatively weak assumptions (valid even in models where gravity is significantly away from GR): that clustering is intrinsically isotropic with respect to the LOS, that in the linear regime growth is scale-independent,⁹ that the Euler equation holds, that gravity is the only force at play on large scales, and that there is no velocity bias of dark matter tracers (galaxies and quasars in this case).

However, the interpretation of this compressed variable as related to the amplitude of matter perturbations, σ_8 , also requires the Poisson equation to hold. As such, this compressed variable does not constrain the matter power spectrum amplitude *per se*, but, for observations at different redshifts, carries information about the growth of structure throughout redshift. Alternatively, within a cosmological model and in combination with the primordial amplitude of perturbations, a primordial power spectrum spectral slope, a theory of gravity and a matter transfer function, it can yield information about the Universe composition and in particular about the matter density parameter. For example in a Λ CDM model, $f(z) = |\Lambda\text{CDM } \Omega_m(z)^\gamma$, with $\gamma \simeq 0.56$ and $\sigma_{s8}(z) \propto D(z)/D(z_i)\sigma_{s8}(z_i)$ where $D(z)/D(z_0)$, depends only on Ω_m . Measurements of $f\sigma_{s8}$ at different redshifts hence constrain Ω_m .

If the true underlying model were instead to be richer than Λ CDM, by interpreting the growth information while adopting the Λ CDM model for $D(z)$, the extracted Ω_m would correspond to a parameter driving the growth of perturbations, which in general for generic gravity models, does not necessarily need to coincide with the background-late-time Ω_m , or the early-time Ω_m , as described in section 3.3. This so-called Ω_m^{growth} is a pure perturbation-late-time quantity. On the other hand, within a Λ CDM model, a constraint on $f\sigma_{s8}$, combined with a constraint on h or k_{eq} (from the BAO or from the shape), leads to a prediction for the amplitude of primordial perturbations. Conversely, a Planck-calibrated Λ CDM model also predicts a value for $f\sigma_{s8}$ as a derived parameter.

It is important to note that the *ShapeFit* compressed variable, $f\sigma_{s8}$, slightly deviates from the traditional approach one, $f\sigma_8$, as explained in detail in [20]. In a nutshell, the deviation is twofold: *i*) *ShapeFit* measures the power spectrum amplitude at a reference scale in units of the sound horizon; and *ii*) upon changing the shape parameter m , only the power spectrum amplitude at the pivot scale $k_p = \pi/r_d$ remains fixed. Therefore, in reality, *ShapeFit* constrains the variable $fA_{sp}^{1/2}$, where A_{sp} is the power spectrum amplitude evaluated at k_p . This quantity can be transformed into our desired compressed variable $f\sigma_{s8}$, considering how deviations from the fiducial template shape choice (i.e., $m \neq 0$) affects the amplitude on scales of $R = 8 \text{ Mpc}/h$,

$$f\sigma_{s8} \simeq f\sigma_{s8}^{\text{fid}} \frac{fA_{sp}^{1/2}}{(fA_{sp}^{1/2})^{\text{fid}}} \times \exp\left(\frac{m}{2a_m} \tanh\left(a_m \ln\left(\frac{r_d^{\text{fid}} [\text{Mpc}/h]}{8 \text{ Mpc}/h}\right)\right)\right), \quad (3.15)$$

where for the *ShapeFit* standard parametrization we have chosen a_m to be 0.6 [20].¹⁰

We illustrate the information that *ShapeFit* $f\sigma_{s8}(z_i)$ measurements add to the geometry and shape in figure 3. The left panel displays the $\Omega_m - h$ plane, similar to both panels of figure 1 combined. Since the additional growth data allow us to constrain the primordial amplitude A_s , we also display the $A_s - h$ plane in the right panel. The colour scheme

⁹If growth were to be scale-dependent the recovered value would correspond to some effective average.

¹⁰Note that eq. 3.15 is not exact, since σ_{s8} is an integrated quantity of the power spectrum, while A_{sp} is not. For that reason it is recommended to always use fA_{sp} for cosmological inference rather than $f\sigma_{s8}$.

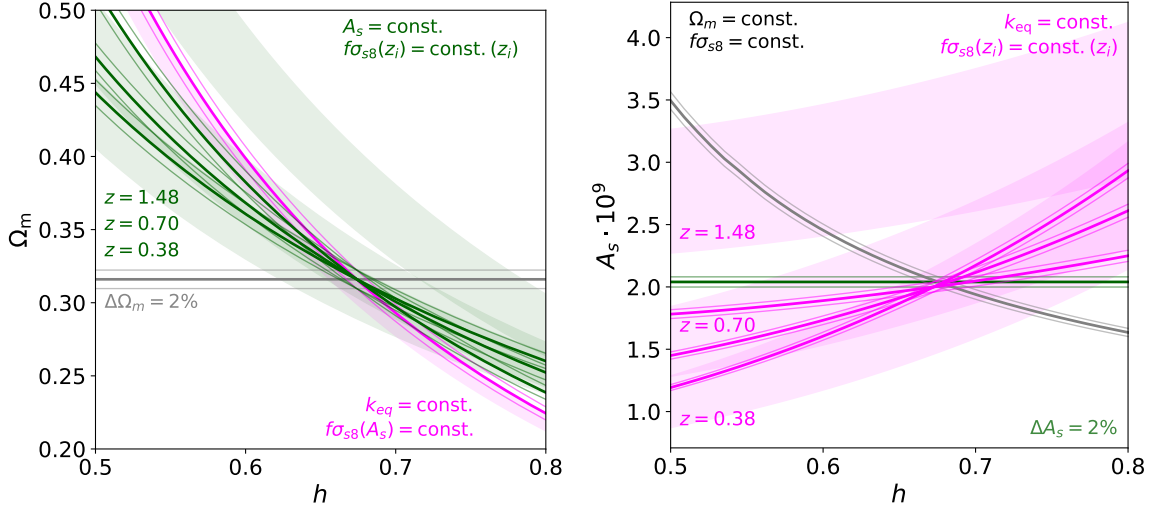


Figure 3. We show the cosmological information encoded in $f\sigma_{s8}$ measurements at three redshift bins. The left and right panels show the $\Omega_m - h$ and $A_s - h$ planes respectively, where thick lines represent those values in parameter space that keep fixed corresponding annotated quantities. In particular, grey lines display fixed Ω_m , magenta lines fixed $k_{\text{eq}} \propto \Omega_m h^2$, and green lines fixed A_s . All lines represent $f\sigma_{s8}$ -isocurves upon considering the full three-dimensional parameter space (Ω_m, A_s, h) . Thin lines indicate 1σ deviations from a Planck-calibrated Λ CDM model and semi-transparent regions show the parameter space constrained by independent late-time probes as specified in the text.

is consistent between both panels, which helps to appreciate the three-dimensionality of the underlying system, $\{\Omega_m, A_s, h\}$. Similarly to previous figures, grey, magenta and green curves keep Ω_m , $\Omega_m h^2$ and A_s fixed, respectively to Planck- Λ CDM reference values, as indicated in the plot. All lines show those parameter combinations that keep $f\sigma_{s8}$ fixed, where in some cases (green lines, $A_s = \text{constant}$) the degeneracy directions are redshift-dependent. All these $f\sigma_{s8} = \text{constant}$ curves are derived from the following scalings for a Planck-like Λ CDM universe,

$$\begin{aligned}
 f\sigma_{s8}(z = 0.38) &= |_{\Lambda\text{CDM}} 0.475 \left(\frac{\Omega_m}{0.316}\right)^{1.76} \left(\frac{h}{0.674}\right)^2 \left(\frac{A_s}{2.04 \times 10^{-9}}\right)^{1/2}, \\
 f\sigma_{s8}(z = 0.70) &= |_{\Lambda\text{CDM}} 0.461 \left(\frac{\Omega_m}{0.316}\right)^{1.52} \left(\frac{h}{0.674}\right)^2 \left(\frac{A_s}{2.04 \times 10^{-9}}\right)^{1/2}, \\
 f\sigma_{s8}(z = 1.48) &= |_{\Lambda\text{CDM}} 0.375 \left(\frac{\Omega_m}{0.316}\right)^{1.22} \left(\frac{h}{0.674}\right)^2 \left(\frac{A_s}{2.04 \times 10^{-9}}\right)^{1/2}.
 \end{aligned} \tag{3.16}$$

The scalings with h and A_s are redshift-independent and arise from the fact that the galaxy power spectrum amplitude scales like $P_g \propto \sigma_8^2 \propto A_s h^4$; the redshift dependence enters through the scaling of Ω_m , which governs the growth history of cosmic structures.

In the left panel of figure 3, the thick grey line refers to constant Ω_m (which can be constrained from a late-time geometry) and the thick magenta line to constant k_{eq} (which is inferred from the *shape* and corresponds to early-time quantities), equivalent to figure 1. The thin lines (for all cases) represent changes in Ω_m by 2%, which correspond to the 1σ sensitivity of Planck within the Λ CDM model. Green thick lines display the combinations of (Ω_m, h)

values that for a given redshift (see the individual relations in (3.16)) keep $f\sigma_{s8}(z)$ fixed, given a constant value of the primordial amplitude A_s . Again, thin green lines represent deviations induced by a variation of Ω_m by 2% around the fiducial value. The green, semitransparent regions show the parameter space constrained at the 1σ level by our *ShapeFit* measurements at redshifts $z = (0.38, 0.7, 1.48)$ (we do not show the $z = 0.51$ bin for better visibility). The $z = 1.48$ bands display a $\sim 2\sigma$ offset value with respect to Planck predictions. This is not unexpected and is caused by the high value of $f\sigma_{s8}$ for the QSO sample in [21] (see also original eBOSS works on this sample [71, 72]).

From the similarity between the theoretical expectation at different redshifts (green curves) alone, we can see that inferring Ω_m from the combination of $f\sigma_{s8}(z)$ measurements is challenging. Also, the green curves are quite similar to the magenta $k_{\text{eq}} \propto \Omega_m h^2$ lines. In fact, for fixed A_s , which fixes the power spectrum amplitude at $k_{\text{piv}} = 0.05 \text{Mpc}^{-1}$, most of the behaviour of $f\sigma_{s8}$ is driven by the exponential term in eq. (3.15) because k_{piv} is rather close to the ‘*ShapeFit* pivot scale’, $k_p \approx 0.03 h \text{Mpc}^{-1}$: most of the amplitude variation at larger wavenumber $\approx 1/(8 \text{Mpc}/h)$ comes from the variation in shape when A_s is fixed. This similarity between k_{eq} and $f\sigma_{s8}$ constraints appears to be stronger for higher-redshifts (where the sensitivity of the growth rate to Ω_m is weaker).

In the right panel of figure 3 we show the behavior of the $f\sigma_{s8} = \text{constant}$ curves in the (A_s, h) plane considering three different cases.

- We keep Ω_m fixed (grey lines), which fixes the growth history, such that the redshift-dependence vanishes. Hence, these lines (where thick lines refer to the fiducial cosmology and thin lines to deviations in A_s by 2%) are identical for each redshift bin.
- We keep $k_{\text{eq}} \propto \Omega_m h^2$ fixed (magenta lines), meaning that Ω_m and hence the growth history changes for varying h . In order to keep $f\sigma_{s8}$ fixed, the change in Ω_m is compensated by varying A_s . Since the impact of Ω_m varies with redshift, this compensation via A_s is redshift-dependent. This is why we show a different magenta isocurve for each redshift. The thin magenta lines represent a variation of A_s by 2%.
- For reference, we also show the case of fixed A_s in green, where thin lines represent, again, a variation of A_s by 2%. It is possible to fix $f\sigma_{s8}$ in this case by adjusting Ω_m as explained before and displayed in the left panel.

In this (A_s, h) plane the redshift dependence of $f\sigma_{s8}$ reveals itself within the $k_{\text{eq}} = \text{const.}$ (magenta) case. Again, we can see the trend that for higher redshifts the green and magenta theory predictions come closer together while for later times the degeneracy is broken: at high- z the compressed variable $f\sigma_{s8}$ is purely determined by the primordial amplitude A_s and the shape $\Omega_m h^2$.

So how does the inclusion of the growth measurements impact our sound-horizon independent measurement of h ? In principle, one could measure h by combining $f\sigma_{s8}$ measurements at different redshifts and derive from figure 3 at which value of h they ‘cross’.¹¹

Considering the (Ω_m, h) plane in the left panel, we can see that, given the BOSS and eBOSS sensitivity (i.e., the size of the semitransparent bands), the combination of growth information from different redshifts cannot efficiently resolve the degeneracy and only provide a very loose constraint on the matter density of $\Omega_m^{\text{growth}} = 0.19 \pm 0.06$. This corresponds to

¹¹Here, it is important to note that by definition the $f\sigma_{s8}$ measurements are independent of the absolute value of the sound horizon. They represent the velocity fluctuation amplitude evaluated at a certain scale in units of the sound horizon, without making any assumption of the absolute value of the sound horizon.

the point in parameter space where all green bands would overlap. As already mentioned, it is not possible to derive h from the growth of structure measurements alone. But, as evident from eq. (3.16), such a measurement can in principle be obtained by using a prior on A_s (and also on n_s , which we do not take into account in this discussion for simplicity). In this way, A_s serves as our new early-time anchor, we hence call the attributed h -measurement h_{A_s} . Such a constraint on h_{A_s} is however very loose: we find an uncertainty of order $\sigma_{h_{A_s}} \approx 0.6$. For that reason we do not consider it in what follows.

On the other hand, the (A_s, h) plane in the right panel reveals an additional h measurement. While h cannot be inferred from $f\sigma_{s8}$ alone, the combination with the measurements of m indeed provides a measurement of h . In particular, we find $h_{m, f\sigma_{s8}} = 0.92^{+0.13}_{-0.18}$, where this high value is driven by the low Ω_m^{growth} measurements given above. Once we combine this with the uncalibrated BAO information we obtain $h_m = 0.701^{+0.019}_{-0.021}$ consistent our h_m measurement from geometry and shape only from section 3.3. In summary, we can see that the addition of growth data amplifies the possibilities for further internal consistency checks of the model:

- In the (Ω_m, h) plane, do the green $f\sigma_{s8} = \text{constant}$ constraints cross at the same position where the magenta m -derived $k_{\text{eq}} = \text{constant}$ constraint crosses the grey Ω_m constraint derived from geometry?
- In the (A_s, h) plane, is the crossing point of the magenta $f\sigma_{s8} = \text{constant}$ constraint consistent with the A_s value that returns the same $f\sigma_{s8}$ given Ω_m is constrained via geometry (grey line)?
- Also in the (A_s, h) plane, is the A_s value inferred from the crossing of the magenta $f\sigma_{s8} = \text{constant}$ constraints and/or their crossing with the Ω_m constraint consistent with the Planck-derived value?

We can see that, once we start including other independent datasets and external priors, this list may become even longer.

One important question in this context is, of course: how could the Λ CDM model be altered or extended to make the model consistent with the higher SH0ES value of the Hubble parameter while preserving agreement with the BOSS+eBOSS sound-horizon-free dataset, in particular our $f\sigma_{s8}$ measurements?

From the left panel of figure 3 we can draw the same conclusion as from figure 1. Without touching the Λ CDM model at or prior to equality, to increase h we need to lower Ω_m , such that the model is still consistent with our k_{eq} and $f\sigma_{s8}$ measurements. But this automatically induces a tension with the (late-time) Ω_m value preferred by geometry. From the right panel we can see that the problem is even more severe: increasing h while still fitting the geometry and growth data forces A_s to decrease. On the other hand, fitting shape and growth data forces A_s to increase. Apparently, the Λ CDM model does not allow us to increase h and at the same time fit the full geometry+shape+growth dataset. A related ‘curiosity’ can be seen from our current BOSS+eBOSS dataset. The high $f\sigma_{s8}$ value reported by the QSO sample pushes Ω_m towards smaller values (and h and A_s towards larger values, where the semitransparent bands overlap), but this is in contradiction with the expected behaviour of a Λ CDM model fed with the best-fitting geometrical constraints of the same QSO sample: a calibrated D_V QSO-only analysis actually yields higher values of Ω_m and lower values of h (see figure 9 of [21]). Since this ‘anomaly’ is not (yet) statistically significant, only future data may allow us to flag this as an inconsistency of the Λ CDM model.

4 Results from BOSS and eBOSS data

4.1 The data

We use the same dataset as in [22] (see table 1 and figure 1 therein). This includes the LRG samples (three redshift bins) covering $0.2 < z < 1.0$ in a wavevector range of $0.02 < k [h\text{Mpc}^{-1}] < 0.15$ pre- and post-reconstruction, as well as the QSO sample (one redshift bin) covering $0.8 < z < 2.2$ in a wavevector range of $0.02 < k [h\text{Mpc}^{-1}] < 0.30$ pre-reconstruction only. We directly use the compressed variables Θ of eq. (3.1) provided by [22], and summarized in appendix E therein. We conveniently transform the compressed datavector (and its covariance) using eqs. (3.2) and (3.3) to obtain the following modified compressed datavector,

$$\Theta'(z) = \{D_V(z)/r_d, F_{\text{AP}}, f(z)\sigma_{s8}(z), m(z)\}. \quad (4.1)$$

We extend the redshift range of our dataset by using the eBOSS DR16 Lyman- α BAO data from [73]. As our baseline choice (that is except in sec. 4.4 where we explicitly vary the number of effective neutrino species), we include the BBN prior adopted from [29, 31, 74],

$$\Omega_b h^2 = 0.02235 \pm 0.00037, \quad (4.2)$$

and fix the spectral index n_s to our baseline choice of,

$$n_s = 0.97. \quad (4.3)$$

In Appendix A we explore the effect of varying these priors. Our cosmological likelihood is based on a modified version of the Boltzmann-code CLASS [75] within the MONTEPYTHON sampler [76].

Unless otherwise stated, we report inference of cosmological parameters obtained from the combination of the constraints on the physical variables at different redshifts. In particular, m is not predicted to change with redshift in any of the Λ CDM extensions considered in this paper; similarly the m measurements reported in [22] do not show any significant redshift-dependence.

4.2 Piecewise- Λ CDM constraints from geometry and shape

As first diagnostic test we present constraints on the matter density Ω_m and the Hubble parameter h under a piecewise-flat Λ CDM model from the different pieces of information introduced in section 3 in figure 4. The left panels show results from the three LRG samples alone ($0.2 < z < 1.0$), while the right panels contain our full LRG+QSO datasets and Lyman- α BAO ($0.2 < z < 3.5$). In this section we explore, how adding different ingredients of the datavector Θ (representing different physical processes) results in different constraints of the model's parameters. We start with the purely geometrical information without BAO calibration (achieved via the sound horizon marginalisation)¹² represented by ' \mathcal{D}_V ' and ' F_{AP} '. The latter alone (grey dotted contours) and its combination with ' \mathcal{D}_V ' (grey solid contours) constrain the matter density Ω_m . Considering only the limited redshift range of LRG only (left panels), the constraints are rather weak ($\sigma_{\Omega_m} \approx 0.05$). Conversely, when considering the full redshift range from all samples (right panels, grey solid contours), the geometrical

¹²This can be achieved by introducing the sound horizon as a nuisance parameter within the cosmological likelihood.

constraint tightens to $\Omega_m = 0.289 \pm 0.016$. Not unexpectedly, the ‘ \mathcal{D}_V ’-derived constraints benefit significantly from the extended redshift range compared to ‘ F_{AP} ’. This is directly related to the fact that ‘ \mathcal{D}_V ’ builds on property *ii*) of the standard ruler definition (see section 3.1), while ‘ F_{AP} ’ does not. These Λ CDM constraints on Ω_m are independent of any early universe assumptions, as the sound horizon information is either cancelled out (grey dotted contours) or marginalized out (grey solid contours). The only assumption entering here is that the late-time background expansion is dictated by standard flat- Λ CDM, hence by Ω_m . Therefore, these represent geometric constraints on the late-time Ω_m^{late} quantity.

Next, we add the sound horizon scale to make use of the full late+early-time information ‘ $D_V/r_d + F_{\text{AP}}$ ’ (light-blue solid contours, lower panels). If the physical baryon density $\Omega_b h^2$ is varied freely, the system would be under-constrained and the light-blue solid contour would become indistinguishable from the grey solid contour. But, by fixing the baryon density via the BBN prior, the system becomes constrained and r_d is ‘calibrated’. Now, $D_V(z)/r_d$ constrains the parameter combinations of eqs. (3.9)-(3.12) displayed via black dashed lines. Together with the uncalibrated BAO constraint on Ω_m , this delivers our first measurement of the Hubble parameter, $h_{r_d} = 0.6742^{+0.0088}_{-0.0094}$, known as the traditional BAO+BBN technique, equivalent to the h -measurement delivered by the eBOSS collaboration team [13], $h = 0.6735 \pm 0.0097$. This measurement relies on the assumptions of standard late-time background expansion, standard pre-recombination physics and that the Ω_m value at pre-recombination times is effectively the same as the late-time one, $\Omega_m^{\text{late}} = \Omega_m^{\text{early,r}}$. This constraint can also be compared with [33] $h = 0.676^{+0.0094}_{-0.0103}$ where the central values are in excellent agreement and the small difference in error-bars arises from a slightly different treatment of the BBN prior and with [21] $h = 0.6742^{+0.0084}_{-0.0091}$.

Finally, we carry out the same exercise (still using the BBN prior), but including the shape measurement $m(z)$ in our cosmological analysis. The shape alone (magenta bands) constrains the parameter combination $\Omega_m h^2$ indicated by the black dash-dotted lines. Combined with the uncalibrated BAO (purely late-time) measurements of Ω_m and using the full LRG+QSO+Lyman- α samples, we find $h_m = 0.695^{+0.042}_{-0.051}$ in the ‘ $F_{\text{AP}} + m$ ’ case (orange contours, upper panels) and $h_m = 0.702^{+0.019}_{-0.021}$ in the ‘ $\mathcal{D}_V + F_{\text{AP}} + m$ ’ case (red contours).¹³ The latter represents our second h -measurement, which is comparable in information content to the sound-horizon-independent constraint of [36–38], although using a larger redshift range and being independent of the Pantheon+ dataset; this can also be compared with the complementary approach and results of [39]. These measurements rely on the assumptions of a standard late-time background expansion, standard matter-radiation equality physics, the fact that r_d is a standard ruler and that the values of Ω_m at equality and late-time are the same, $\Omega_m^{\text{early,eq}} = \Omega_m^{\text{late}}$.

Consistently combining these two measurements we obtain the full BAO+BBN+shape constraint $h_{(m,r_d)} = 0.6790^{+0.0076}_{-0.0075}$ (‘ $D_V/r_d + F_{\text{AP}} + m$ ’ case), which relies on standard late-time background expansion, standard pre-recombination and equality epoch physics, and that Ω_m is the same in all those epochs, $\Omega_m^{\text{late}} = \Omega_m^{\text{early,r}} = \Omega_m^{\text{early,eq}}$. As appendix A shows, while the adopted baryon abundance prior is important for h (but not for Ω_m), a reasonably wide prior on n_s has a small effect on both parameters.

The individual h -measurements are summarized in table 1 (the full results are reported in appendix B, table 3). We see that under the assumption of the flat Λ CDM model and

¹³Note that the sound horizon marginalisation applied to obtain the uncalibrated BAO also changes the pivot scale k_{sp} at which the shape m is defined. We find that this does not impact our h_m measurement, since m represents an almost scale-independent slope (see also [37] for a more detailed discussion).

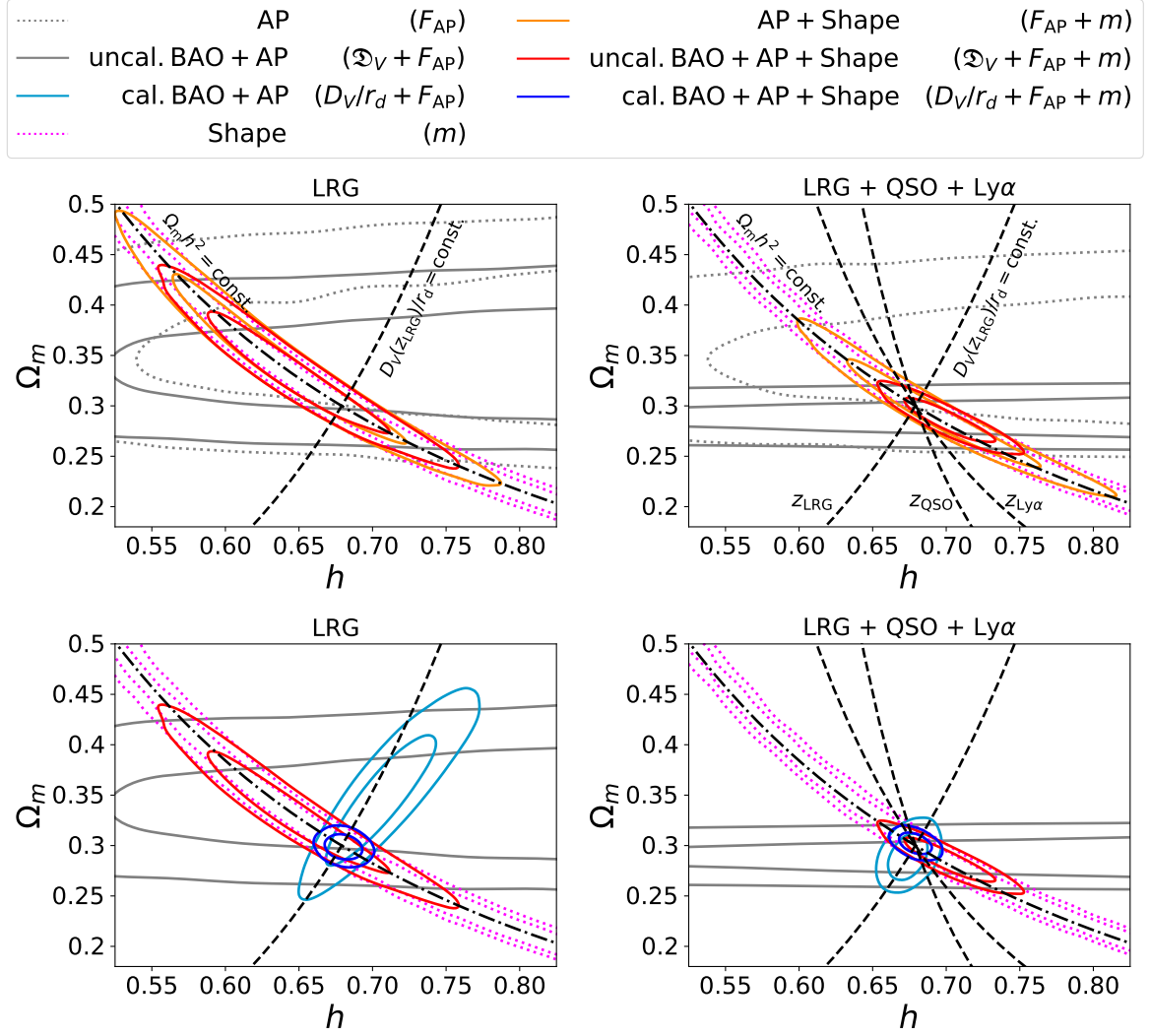


Figure 4. $\Omega_m - h$ plane derived from piecewise Λ CDM fits to the BOSS+eBOSS LRGs (left panels) and all samples (right panels) considering different combinations of compressed variables. The upper panels show all constraints except the ones relying on BAO calibration, which are shown in the lower panels only. Grey contours refer to purely late-time constraints, either only using the AP parameter, F_{AP} (grey dashed contours, upper panels), that does not assume any information on the sound horizon scale physics (only its existence as an isotropic feature), or combining F_{AP} with the uncalibrated BAO information, \mathfrak{D}_V , standing for D_V/r_d with r_d marginalised out (grey solid contours), which additionally assumes that r_d does not change with redshift. These results (grey curves), by construction, are independent of the employment of any BBN prior. Note, however, that all colored lines assume BBN (not included in the legend for conciseness). By adding information on the absolute size of r_d we obtain our first measurement of h (light-blue contours), commonly known as BAO+BBN. On the other hand, the shape m alone (magenta dash-dotted line) constrains the combination of $\Omega_m h^2$ (upon priors on n_s and $\Omega_b h^2$ are set). By adding either the F_{AP} (orange contours) or $F_{\text{AP}} + \mathfrak{D}_V$ (red contours) information on Ω_m , we obtain sound-horizon-independent constraints on h . All combined (dark-blue contours) give the full BAO+BBN+shape result for h . All these h -measurements are provided in table 1.

the employed BBN prior, all these measurements are consistent with each other. In fact, the two degeneracy directions (that enable our two h -measurements) displayed by the black dashed and dash-dotted lines in figure 4, exactly meet where they are in agreement with the Ω_m band obtained from the expansion history. On one hand this indicates the strong self-consistency of the Λ CDM model. On the other hand this exemplifies how difficult it is to reconcile the high- h value obtained by SH0ES, $h = 0.7304 \pm 0.0104$ [7], with indirect determinations of h by postulating new physics in the early Universe. Any extension to the standard model must consistently change the sound horizon and the matter-radiation equality physics, in such a way that both ‘anchors’ deliver a SH0ES-consistent value for h , as well as a consistent Ω_m measurement with the uncalibrated late-time universe measurements. Indeed this is what [39] finds for a range of popular beyond- Λ CDM models. Looking forward, as the error-bars continue to shrink, this implies that a new value of h cannot be reached by moving along one of the two degeneracy directions displayed in figure 4; nor it can be achieved by recalibrating or changing either the length of the sound horizon scale, or the interpretation of the shape. Instead, to accommodate a significantly higher value of the Hubble parameter, both degeneracy directions must be coherently shifted towards higher values of h . This implies that the physics governing the sound horizon at radiation drag (as seen in the BAO) and the physics governing the shape, hence to first approximation physics around matter-radiation equality, should be changed in a coherent manner as not to disturb the (currently evident) agreement. Alternatively, two different mechanisms would need to be invoked, one (early-time) that shifts r_d and another one completely unrelated that shifts m ‘just so’ to preserve the agreement. This agreement also includes obtaining a consistent Ω_m value with respect to that delivered by the uncalibrated BAO, based entirely on geometric late-time physics and the early-time one.

These considerations can be seen as a straitjacket for extended models that could potentially resolve the Hubble tension.

4.3 Piecewise Λ CDM constraints from geometry, shape and growth

We investigate how adding the growth signal affects measurements of h . Adding the (relative) growth signal does not change the h -anchor, so this route provides effectively another determination of the same quantities as above, h_m , h_{r_d} or $h_{(m,r_d)}$. As explained in section 3.4, the *ShapeFit* $f\sigma_{88}(z)$ measurements carry two types of information: 1) the global amplitude of perturbations, which is given by the scalar amplitude A_s of fluctuations generated by inflation, and by h through the units of σ_{88} in $\text{Mpc}h^{-1}$; and 2) the *relative* redshift evolution of $f\sigma_{88}(z)$, which only depends on the matter density Ω_m within a flat- Λ CDM model (see equations 3.16). Note that since in our baseline setup we vary A_s freely, we can only constrain Ω_m through the *relative* redshift dependence of $f\sigma_{88}$ across redshift bins, which is, by construction, independent of the overall scalar amplitude A_s . On the other hand, the variation of A_s does not allow us to obtain a third independent h measurement, as the system still needs to be calibrated, either through m or the sound horizon scale, as we have described in section 4.2. Note that in this case, the intrinsic Λ CDM assumption of $\Omega_m^{\text{growth}} = \Omega_m^{\text{late}}$ or $\Omega_m^{\text{growth}} = \Omega_m^{\text{early}}$ will be exploited.

The resulting constraints on the flat- Λ CDM parameters are displayed in figure 5 for the whole set of BOSS+eBOSS tracers (LRG+QSO+Lyman- α ; $0.2 < z < 3.5$), for different combinations of parameters (analogously to the right panels of figure 4, but all including $f\sigma_{88}$). As before, some of the parameter combinations require either a prior on the baryon density, or the spectral index, exactly in the same way as previously described in section 4.2,

H_0 [km s⁻¹ Mpc⁻¹] \pm 68% CL

Probe/feature	LRG	ALL	Assumptions
$F_{\text{AP}} + m$ (h_m)	$63.9^{+4.7}_{-6.4}$	$69.5^{+4.2}_{-5.1}$	$\Omega_m^{\text{eq}} = \Omega_m^{\text{late}}$ & i); priors on ω_b, n_s
$\mathcal{D}_V + F_{\text{AP}} + m$ (h_m)	$64.5^{+3.5}_{-4.5}$	$70.1^{+2.1}_{-2.1}$	i), ii); priors on ω_b, n_s
$D_V/r_d + F_{\text{AP}}$ (h_{r_d})	$70.8^{+2.2}_{-2.8}$	$67.42^{+0.88}_{-0.94}$	$\Omega_m^r = \Omega_m^{\text{late}}$ & i), ii), iii); prior on ω_b
$D_V/r_d + F_{\text{AP}} + m$ (h_{m,r_d})	$67.99^{+0.83}_{-0.85}$	$67.90^{+0.76}_{-0.75}$	i), ii), iii); priors on ω_b, n_s
$F_{\text{AP}} + m + f\sigma_{s8}$	$63.8^{+4.5}_{-5.8}$	$72.8^{+4.0}_{-4.8}$	$\Omega_m^{\text{eq}} = \Omega_m^{\text{late}}$ & i), GR; priors on ω_b, n_s
$\mathcal{D}_V + F_{\text{AP}} + m + f\sigma_{s8}$	$64.5^{+3.5}_{-4.5}$	$70.2^{+1.9}_{-2.1}$	i), ii), GR; priors on ω_b, n_s
$D_V/r_d + F_{\text{AP}} + f\sigma_{s8}$	$70.9^{+2.2}_{-2.8}$	$67.37^{+0.86}_{-0.95}$	$\Omega_m^r = \Omega_m^{\text{late}}$ & i), ii), iii), GR; prior on ω_b
$D_V/r_d + F_{\text{AP}} + m + f\sigma_{s8}$	$68.00^{+0.73}_{-0.73}$	$67.9^{+0.76}_{-0.75}$	i), ii), iii), GR; priors on ω_b, n_s

Table 1. Constraints for the Hubble expansion rate, $H_0 = 100h$ [km s⁻¹ Mpc⁻¹], considering different combinations of compressed variables from either LRGs only ($0.2 < z < 1.0$) or all samples combined ($0.2 < z < 3.5$) and different anchors. The top two rows show constraints on H_0 independent of the sound horizon, whereas the two rows below include the calibrated BAO. The four bottom rows report those constraints including the $f\sigma_{s8}$ variable (first two independent of sound horizon, second two with the calibrated sound horizon scale), which additionally assume GR at the perturbation level. Adding the growth information does not change the anchor, of course. All results are based on the flat Λ CDM model assumption (at the background level) and include the BBN prior from eq. (4.2). Those results including the shape parameter m also include the n_s prior from eq. (4.3). The assumptions i), ii), iii) have been introduced in section 2. All results are graphically displayed in figure 4 (four top rows) and figure 5 (three bottom rows, for ‘ALL’ only).

and as explicitly displayed in the right column of Table 1. The information is split in two panels, where the right panel is a zoom into the left panel, which allows for a comparison of our ShapeFit constraints with Planck.

The addition of the $f\sigma_{s8}$ constraint does not change significantly the constraints on Ω_m or h . Nevertheless it is interesting to note that, in principle, if $f\sigma_{s8}$ could be measured over a wide redshift range and with enough accuracy, the combination $m + f\sigma_{s8}$ could yield a qualitatively different h determination whereby the $\Omega_m h^2 = \text{constant}$ degeneracy given by m is broken by a determination of Ω_m^{growth} that only relies on the growth of perturbations. For the redshift range available, with baseline from $z = 0.38$ to $z = 1.48$, and at the current precision level, this is not yet possible. However, forthcoming data and the addition of higher-order statistics may be able to break the degeneracy between f and σ_{s8} [77] making this new h determination possible.

To summarize, when the $f\sigma_{s8}$ information is combined with the calibrated BAO, or the uncalibrated BAO+shape, h is fully determined, and $f\sigma_{s8}$ moderately helps to increase the precision of the h determination. These measurements allow for an extra determination of

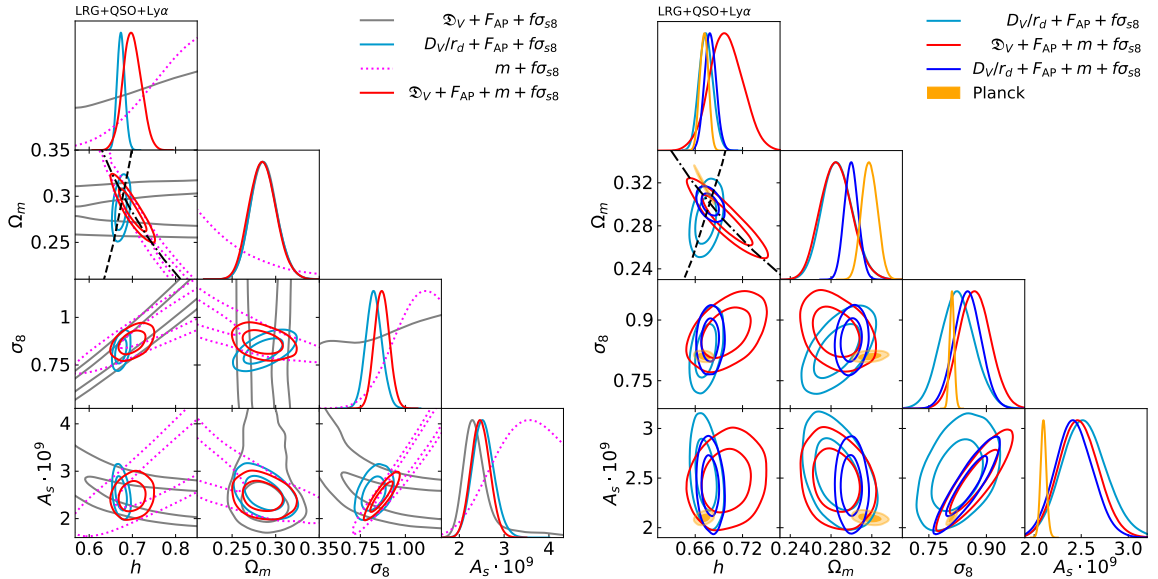


Figure 5. Derived constraints from piecewise Λ CDM fits to the BOSS+eBOSS samples (LRG+QSO+Lyman- α), analogous to the right plots

of figure 4, using the same colour scheme. The right panel is a zoom into the left panel, where we also show the full ShapeFit (empty dark-blue contours) and Planck [9] Λ CDM (filled orange contours) constraints. All cases include the perturbation-like variable $f\sigma_{88}$, which allow us to set constraints on the amplitude of perturbations (σ_8 or A_s) when the GR assumption is being made to connect the matter at background and perturbation levels:

$\Omega_m(z) = f(z)^{0.56}$. The black dashed lines in the $\Omega_m - h$ panels are the same as those in figure 4. Priors on $\Omega_b h^2$ and n_s are set when they are relevant, according to eqs. (4.2) and (4.3), respectively. The Hubble parameter can be constrained efficiently only if either the system is calibrated using the sound horizon scale as a ruler, or the shape parameter, m , is employed to determine how fast the horizon grows at matter-radiation equality epoch. Thus, adding the perturbation information through $f\sigma_{88}$ only helps to improve the constraints on h via an improvement on the Ω_m determination. In principle a determination of h based on $m + f\sigma_{88}$ would also be possible, but in practice $f\sigma_{88}$ alone constraints Ω_m poorly, in part

due to the lack of precise measurements at very distinct redshifts. As in figure 4 all h constraints are fully consistent. These constraints are reported in table 1 and table 3.

h which relies on the Λ CDM assumptions: 1) the growth of structure is connected to the matter density according to GR predictions; 2) this perturbation-derived matter density is the same as the late-time-background density, or also additionally to the early-time matter density. However, note that these ‘new’ values of h so obtained are fully correlated with those described in section 4.2.

The bottom two rows of both panels of figure 5 are useful to shed light on another mild tension involving σ_8 , the late-time amplitude of perturbations (see [40] and references therein). In particular, weak-lensing observations (for e.g., [78]) tend to report a lower value of σ_8 compared to that estimated from CMB data [9]. The constraints reported in figure 5, which include the redshift space distortion information through $f\sigma_{88}$, enable another diagnostic test or internal consistency check. Moreover, any proposed solution to fix the Hubble tension should also help to improve, or at least not exacerbate, the σ_8 tension.

For example, the $m + f\sigma_8$ constraint (combining equality physics with late-time growth rate) would need a higher A_s for higher h values, but also higher σ_8 values. On the other hand, the purely late-time, uncalibrated BAO signal, combined with the growth rate constraints, would need a lower A_s for higher values of h , but also a lower σ_8 . This type of ‘scissor’ behaviour of the constraints is particularly useful for diagnostic tests of the model.

By combining the un-calibrated BAO information with the shape and relative growth, we obtain a σ_8 value of $\sigma_8 = 0.872^{+0.042}_{-0.042}$ (red lines). This result relies upon the velocity at which the modes re-enter the horizon at matter-radiation scales, and other late-time quantities (growth and geometry), but is independent of sound-horizon scale physics. On the other hand, the sound horizon scale calibrated results (cyan lines) in combination with $f\sigma_8$ yield a highly consistent value $\sigma_8 = 0.825^{+0.043}_{-0.047}$. This determination is also highly consistent with the official eBOSS reported value, $\sigma_8 = 0.850^{+0.033}_{-0.033}$ [13]. The full combination of sound-horizon calibrated BAO of LSS and the shape m , relying on processes at equality, and the late-time growth rate, provides $\sigma_8 = 0.850^{+0.035}_{-0.038}$, again very similar to the eBOSS official results. The values of σ_8 , as well as other parameters of interest are reported in Appendix B, table 3.

4.4 Beyond Λ CDM: massive neutrinos and dark-radiation.

Two popular Λ CDM extensions involve considering a free sum of neutrino masses parameter, Σm_ν , or varying the effective number of neutrino species, N_{eff} , incorporating dark radiation. We explore the constraints *ShapeFit* impose on h within these models.

The effect of varying the sum of the neutrino masses is displayed in the left panel of figure 6 for the geometry, shape and growth parameters, as in figure 5, using the same colour scheme. For comparison, the dotted lines are the constraints for a standard Λ CDM model. Interestingly, varying the sum of neutrino masses has a very distinct effect on the constraints provided by the different features used by *ShapeFit*. Features that depend on the sound horizon yield cosmological parameters degeneracy directions (cyan contours) very different from those obtained considering features that depend on the shape (red). A large Σm_ν forces h to decrease (increase) for the sound horizon (shape) physical parameters combinations, implying that a large value of Σm_ν cannot solve the h tension. Both cases consistently overlap at $h = 0.6786^{+0.0078}_{-0.0074}$ (and Σm_ν consistent with zero), consistent with Planck low- h values. A similar effect appears for σ_8 , where the constraints based on the sound horizon ruler (shape) tend to have lower (higher) values of σ_8 , although both are consistent with the combined preferred value $\sigma_8 = 0.853^{+0.035}_{-0.036}$. This ‘scissor’ behaviour offers a useful diagnostic test of the model.

Next, in the right panel of 6 we show the effect of additional dark radiation, parameterised by the effective number of neutrino species N_{eff} . We include the BBN prior, but we adjust our baseline choice of eq. (4.2) taking into account the BBN constraints on $\Omega_b h^2$ and N_{eff} when considering Deuterium [74] and Helium [79] data (see figure 1 in [32]). For simplicity, instead of undertaking the full BBN likelihood calculation as in [33], we choose the following Gaussian priors

$$\Omega_b h^2 = 0.0222 \pm 0.0005 \quad N_{\text{eff}} = 3.0 \pm 0.3, \quad (4.4)$$

where we also incorporate a correlation coefficient between both parameters of $\rho = 0.6$ to correctly reproduce the findings of [32].

Again, we show the constraints obtained from geometry and growth (cyan contours), shape and growth (red contours), and their combination (blue contours). The Λ CDM degeneracies discussed extensively in section 3.3 are also indicated here via the black lines in the

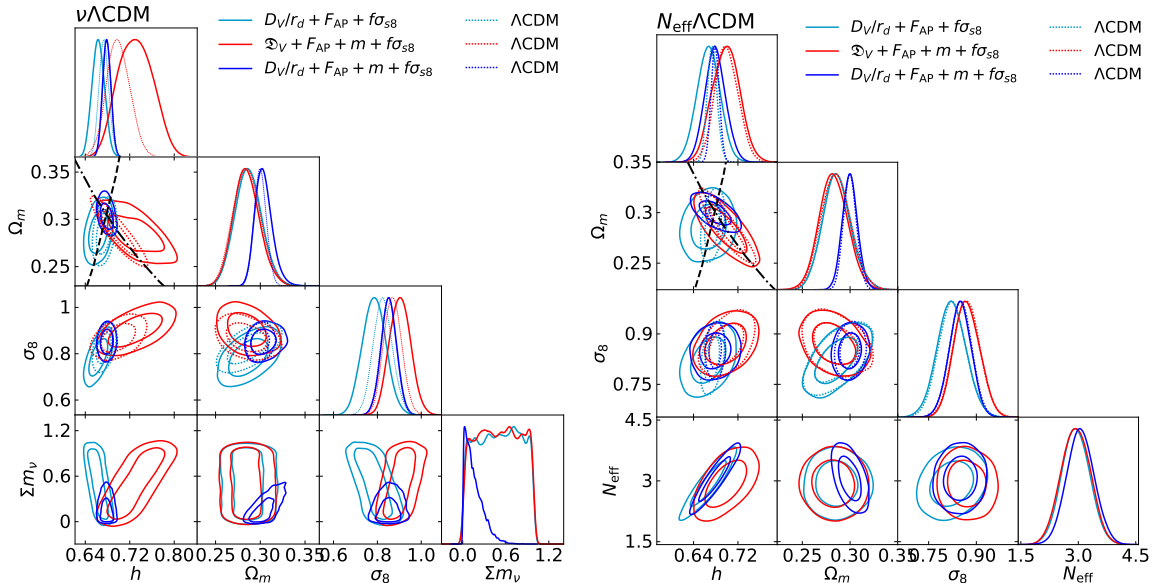


Figure 6. Left panel: parameters of the $\nu\Lambda\text{CDM}$ model (with a BBN prior) for the most relevant cases when the shape, geometry and growth parameters have been added on the BOSS+eBOSS samples ($0.2 < z < 3.5$), following the same colour scheme as in the previous figures. When the $\sum m_\nu$ parameter space is varied, a degeneracy with h appears. However this $\sum m_\nu - h$ degeneracy is different when using the sound horizon scale anchor (cyan contours) and when using the shape parameter m : higher neutrino masses prefer a lower (higher) value of h for the sound horizon (shape) informed analysis. This ‘scissor’ behaviour is precisely which allows to break the degeneracy and put moderate constraints on $\sum m_\nu$ without needing any other external dataset (such as CMB data). A uniform prior of $0 < \sum m_\nu < 1$ has been applied in all cases. Right panel: parameters of the $N_{\text{eff}}\Lambda\text{CDM}$ model (with a BBN prior) for the same cases and same colour scheme as in the left panel. We adopt priors on $\Omega_b h^2$, N_{eff} provided in eq. (4.4) motivated by the full BBN treatment of [33].

(Ω_m, h) plane. We can see that, despite the inclusion of dark radiation, the posteriors are still restricted to these degeneracies. The posterior widths inflate, subject to the fact that the BBN prior now allows for a certain correlation between $\Omega_b h^2$ and N_{eff} [32, 33]. In particular, we measure $h_{r_d} = 0.667 \pm 0.021$ in the geometry and growth case; $h_m = 0.699 \pm 0.025$ in the shape and growth case, and $h_{m,r_d} = 0.679 \pm 0.019$ in the combined case (for full results see appendix B, table 3).

Figure 7 summarizes the different values of h ’s obtained in this section, where the colour code follows that of figures 4-6. The first upper panel shows the results summarized in section 4.2 based exclusively on background geometry and shape; the second panel displays the results described in section 4.3, which consists of adding the growth information. Both upper panels display the h results for a flat- ΛCDM model. The two bottom panels display the results based as well on background (geometry and shape) and perturbation (growth), for the $\nu\Lambda\text{CDM}$ and N_{eff} models as described in this section. We also include the light-blue and grey bands, corresponding to the measurements of Planck [9] and SH0ES [69], respectively. In general, measurements calibrated with the horizon scale (cyan symbols) are in good agreement with the low- h value measured by Planck, whereas the shape-informed measurements (red) is, given the error-bars, consistent with both.

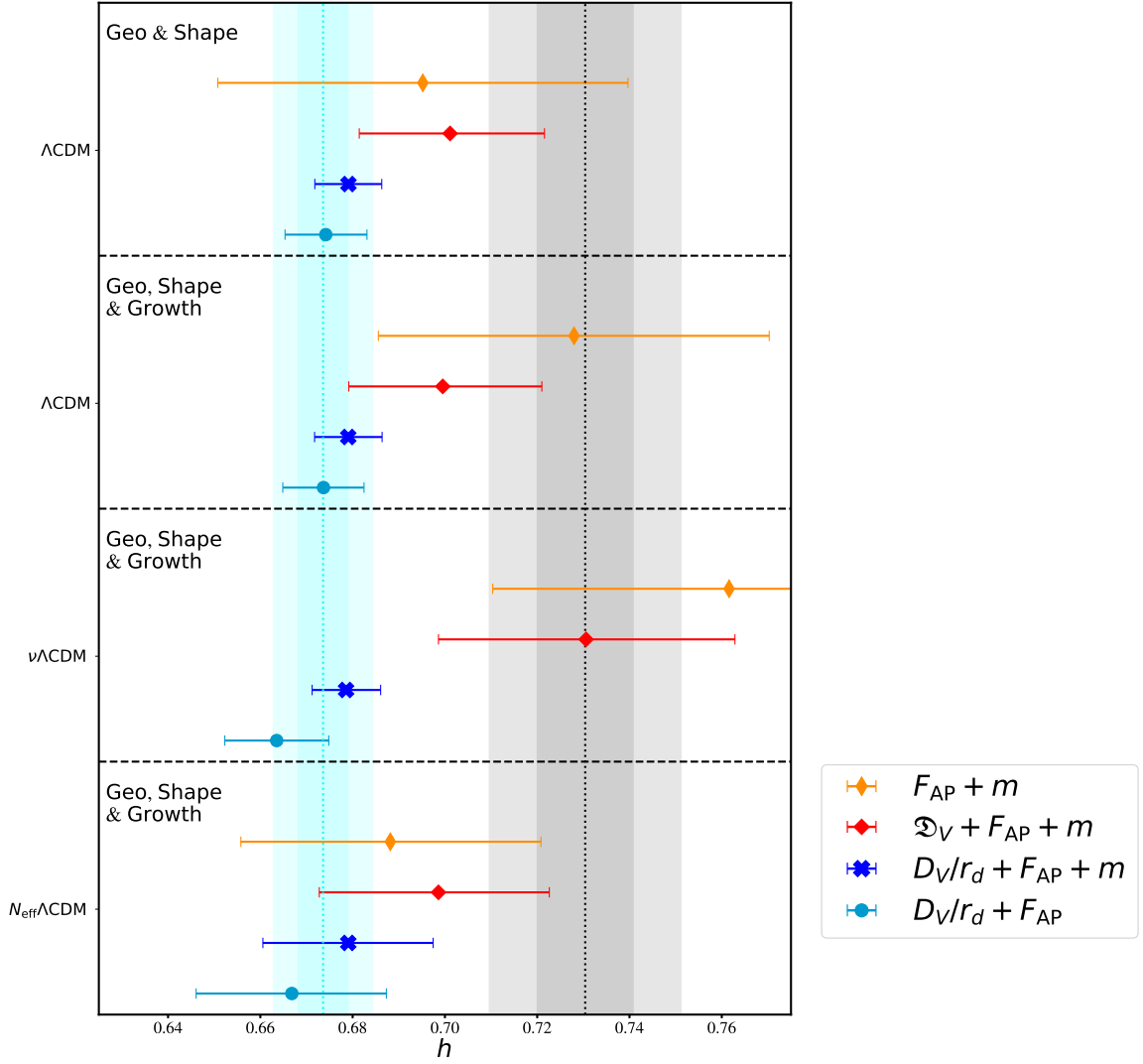


Figure 7. Summary plot of the most relevant results on h of section 4 obtained from BOSS and eBOSS data in combination with a BBN prior on $\Omega_b h^2$ and with n_s set to 0.97. The top and middle panels display the results for a Λ CDM model when geometry and shape parameters are used (background variables only $D_V/r_d, F_{\text{AP}}, m$) and when the growth is also added (perturbation variable, $f\sigma_{88}$), respectively. The two bottom panels display the same results for two extra cosmologies, a $\nu\Lambda$ CDM and $N_{\text{eff}}\Lambda$ CDM, when geometry, shape and perturbation variables are considered. The symbols, whose errors represent the 1σ confidence level, follow the same colour scheme described in figures 4-6. Additionally, the constraints from Planck [9] and SH0ES [69] have been added as light-blue and grey bands, for the 1σ and 2σ confidence levels. The relatively large central value for the orange constraints in the two central panels is driven by the high $f\sigma_{88}$ for the quasars sample (see figure 3). This is not reflected in the red constraints, in which most of the impact on h coming from the Ω_m determination from $f\sigma_{88}$ is heavily superseded by the one from $\mathcal{D}_V + F_{\text{AP}}$.

5 Beyond m - a geometrical interpretation of the shape.

As indicated already in section 3.2, our h_m measurement based on the equality scale is indeed independent of the absolute value of the sound horizon r_d , but still makes use of the fact that

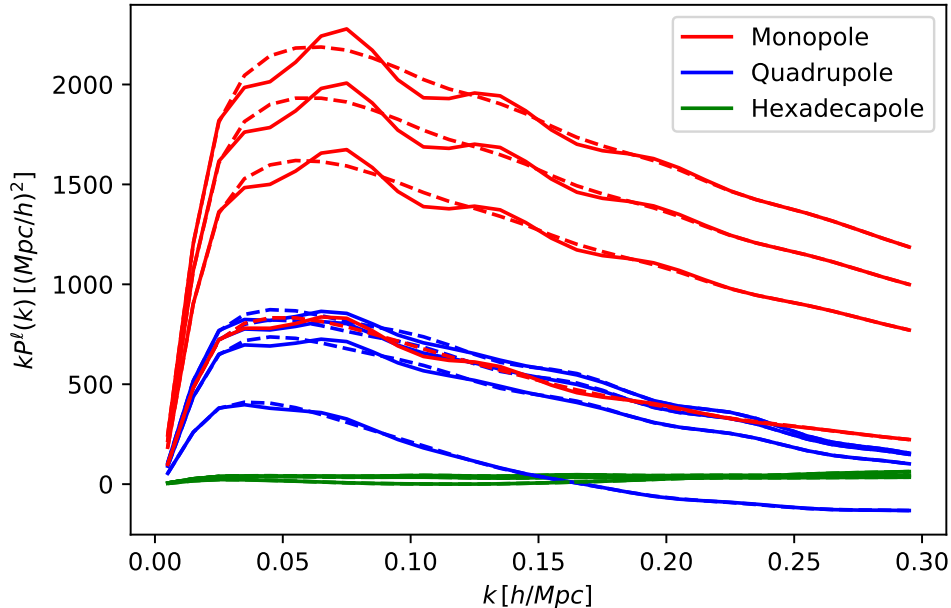


Figure 8. Linear theory prediction for the galaxy power spectrum multipoles at the four considered eBOSS redshift bins (from lowest redshift bin at top to highest redshift bin in the bottom) used to generate our mock dataset. Solid lines include the BAO wiggles (‘withBAO’), while they are removed for the dashed lines (‘noBAO’).

r_d is a standard ruler (in order to provide a constraint on Ω_m). In this section we would like to explore the option of using instead the direct measurement of the equality scale k_{eq}^{-1} itself (from the turnover of the power spectrum) as a standard ruler. Then we investigate how this characteristic scale relates to the shape parameter m , and a potential additional measurement of h .

5.1 Mock analysis setup

For this purpose, we create a mock dataset, ‘withBAO’, coinciding with the linear theory prediction of the galaxy power spectrum multipoles $P^\ell(k)$ for the fiducial eBOSS cosmology and galaxy bias (motivated by table F3 of [80]) at each redshift bin centered at $z = \{0.38, 0.51, 0.70, 1.48\}$, which we refer as LRG+QSO sample. Another mock data set, ‘noBAO’, is created using the same parameters, but with BAO wiggles removed using the numerical smoothing method provided in appendix D of [22]. The theory prediction used to produce these idealized set of mocks are displayed in figure 8. When analysing this set of mocks we employ the same covariances as for the original BOSS and eBOSS data.

For the fixed-template fits we assume the same model that has been used to generate the mock power spectra: we use linear perturbation theory, the second order bias expansion parameterized by b_1, b_2 in the same way as in [22, 80] and assume the non-local bias parameters $b_{s,2}, b_{3\text{nl}}$ to follow the local Lagrangian predictions [81, 82]. We incorporate the redshift-space distortion via the Taruya-Nishimichi-Saito (TNS) model [83] and a Lorentzian Fingers-of-God (FoG) damping term parameterized by the dispersion scale σ_{FoG} . Finally, we model deviations

from Poissonian shot noise via the parameter A_{noise} as defined in [22]. For all samples we fit the wavevector range $0 < k \text{ [hMpc}^{-1}] < 0.15$.¹⁴ We analyse each set of mocks as follows.

- ‘withBAO’. Using the fiducial linear power spectrum as template, we apply both *ShapeFit* and the classic fit (where m is kept to be fixed to 0) to each redshift bin varying the physical parameters $\{\alpha_{\parallel}, \alpha_{\perp}, f, (m)\}$ and the nuisance parameters $\{b_1, b_2, \sigma_P, A_{\text{noise}}\}$.
- ‘noBAO’. Using the dewiggled linear power spectrum as template, we apply both *ShapeFit* and the classic fit to each redshift bin consisting of the physical parameters $\{\alpha_{\parallel}, \alpha_{\perp}, f, (m)\}$ and the same nuisance parameters as above.

In the ‘withBAO’ case the physical parameter constraints can be interpreted in the usual way (see section 3.3 of [51] for a concise overview). In particular, the scaling parameters $\{\alpha_{\parallel}, \alpha_{\perp}\}$ can be transformed easily to the parameter base Θ introduced in eq. (3.1) via

$$\frac{D_H(z)}{r_d} = \alpha_{\parallel}^{\text{withBAO}} \frac{D_H^{\text{fid}}(z)}{r_d^{\text{fid}}}, \quad \frac{D_M(z)}{r_d} = \alpha_{\perp}^{\text{withBAO}} \frac{D_M^{\text{fid}}(z)}{r_d^{\text{fid}}}. \quad (5.1)$$

However, in the ‘noBAO’ case the interpretation of the scaling parameters $\{\alpha_{\parallel}, \alpha_{\perp}\}$ needs to be modified, since the sound horizon is not a measurable quantity anymore. Instead, the equality scale earns the role of a standard ruler, such that the physical interpretation of the generic scaling parameters changes to

$$\frac{D_H(z)}{k_{\text{eq}}^{-1}} = \alpha_{\parallel}^{\text{noBAO}} \frac{D_H^{\text{fid}}(z)}{(k_{\text{eq}}^{-1})^{\text{fid}}}, \quad \frac{D_M(z)}{k_{\text{eq}}^{-1}} = \alpha_{\perp}^{\text{noBAO}} \frac{D_M^{\text{fid}}(z)}{(k_{\text{eq}}^{-1})^{\text{fid}}}. \quad (5.2)$$

Any cosmological BAO likelihood can be adjusted to the equality-based formulation of eq. (5.2), simply by replacing the sound horizon by k_{eq}^{-1} .

5.2 Compressed-variables results

The compressed results of the four fits are shown in the left panel of figure 9: ‘withBAO *ShapeFit*’ (filled blue contours), ‘withBAO classic’ (filled green contours), ‘noBAO *ShapeFit*’ (empty blue contours), and ‘noBAO classic’ (empty green contours), for the eBOSS LRG sample at effective redshift $z = 0.70$ (recall that the error-bars have been derived by assuming the actual eBOSS LRG covariance on these mocks). The right panel is a zoom-in of the left panel, but without the ‘noBAO *ShapeFit*’ case. Note that the physical interpretation of the scaling parameters is different between the ‘withBAO’ and ‘noBAO’ cases, according to eqs. (5.1) and (5.2). The fact that the filled contours are tighter than the empty contours, reveals that –within the standard ruler analysis– the equality scale is significantly less constraining than the sound horizon. This is expected, as the BOSS and eBOSS galaxy power spectra are not very sensitive to the turnaround scale $k_{\text{eq}} \sim 0.01 \text{ [hMpc}^{-1}]$, even in our optimistic case without a scale cut on the minimum k (and fully systematics-free). Instead, they are sensitive to the broadband shape for scales $k > k_{\text{eq}}$. Note that the green dashed lines have m fixed at the fiducial value, in the blue dashed lines m is a free parameter. The skewed and asymmetric constraints shown by the blue dashed lines are due to a combination of a non-linear response of the likelihood to changes in m around the fiducial value and to prior volume effects.

This is the reason why we observe such a strong correlation between the scaling parameters $\{\alpha_{\parallel}, \alpha_{\perp}\}$ and m in the ‘noBAO *ShapeFit*’ case, in which these parameters remain unconstrained, meaning that the cosmological interpretation of m and D_V/k_{eq}^{-1} are indeed closely related.

¹⁴Note that for the actual BOSS and eBOSS data we always set $k_{\text{min}} = 0.02 \text{ hMpc}^{-1}$.

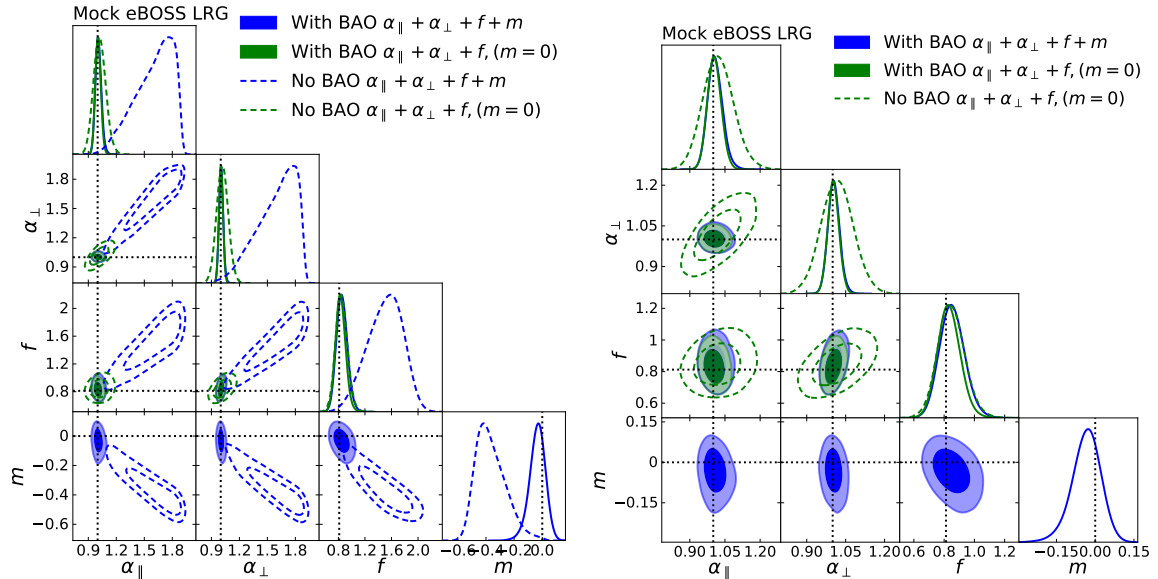


Figure 9. Tests on mocks: Fixed-template bestfit parameters for the mock power spectra of figure 8, corresponding to the eBOSS LRG sample at effective redshift $z = 0.70$. The physical parameters $\{\alpha_{\parallel}, \alpha_{\perp}, f, m\}$ constraints for the fixed template fits to the ‘withBAO’ and ‘noBAO’ are represented by filled and empty contours, respectively. The fit including m is shown in blue, the other two fits, where m has been fixed to its fiducial value, are shown in green. The right panel is a zoom-in of the left panel, with the ‘noBAO *ShapeFit*’ case excluded. The black dotted lines indicate the ‘true’ parameter values, from which the mocks were generated.

5.3 Cosmological interpretation of the mock data

We explore how the compressed mock data results compare in light of a flat Λ CDM model. We fix n_s to the underlying value and use a prior on $\Omega_b h^2$ with the same width as in eq. (4.2), but centered around the underlying value. Using eqs. (5.1) and (5.2) for the different sets of scaling parameters, we obtain the constraints on Ω_m and h shown in figure 10.

First, we show the results from interpreting m only in the ‘withBAO’ case (magenta contour). This constraint exactly follows the relation $\Omega_m h^2 = \text{const.}$ indicated (for the true cosmology) by the black dash-dotted line: it is the same behaviour already observed in figure 4. The filled green (blue) contours show the ‘withBAO’ results from the scaling parameters via eq. (5.1), excluding (including) the shape. The empty green dashed contours arise from interpreting the scaling parameters in the ‘noBAO’ case via eq. (5.2). Interestingly, they do not overlap with the ‘withBAO’ m -only constraints, but approximately follow the combination $\Omega_m h = \text{const.}$, indicated by the black dashed line that represents the limit $z \rightarrow 0$. The grey region indicates how this line evolves across redshifts.

This behavior can be explained as follows. The wavevector of equality k_{eq} in units of $1/\text{Mpc}$ is proportional to

$$k_{\text{eq}} \propto \Omega_m h^2, \quad (5.3)$$

which is what m measures through the *feature* associated to the wavevector of equality: the broadband shape. In the ‘noBAO’ case, however, the scaling parameters are not sensitive to the absolute scale of equality k_{eq}^{-1} , but to the cosmological distance in units of the equality scale (see eq. (5.2)). Assuming the low redshift limit $z \rightarrow 0$, where all cosmological distance are

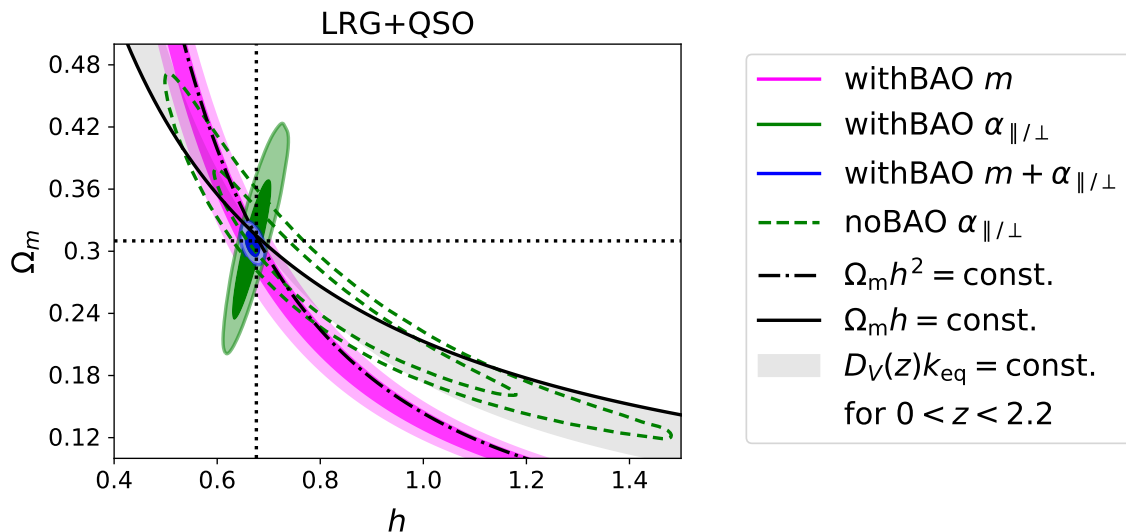


Figure 10. Interpretation of the results of the compressed variables in figure 9 for a flat- Λ CDM model assumption. We employ the same colour code, but this time also adding in magenta the ‘withBAO m ’ results from m -only. These follow the $\Omega_m h^2 = \text{const.}$ line indicated by the black dash-dotted line, while the k_{eq}^{-1} -derived constraints (empty green dashed contours) correspond to $D_V(z)k_{\text{eq}} = \text{const.}$ (grey region), where the $z \rightarrow 0$ limit, $\Omega_m h = \text{const.}$, is indicated by the black solid line. The underlying values used to generate the power spectrum mock signal are shown by the horizontal and vertical black dashed lines.

proportional to the inverse Hubble parameter, $D \propto 1/h$, we find the following proportionality in the ‘noBAO’ case,

$$\frac{D}{k_{\text{eq}}^{-1}} = Dk_{\text{eq}} \propto \frac{\Omega_m h^2}{h} = \Omega_m h . \quad (5.4)$$

In reality, cosmological distances at non-zero redshifts show the additional Ω_m -dependence of eqs. (3.5)-(3.8), represented by the grey semitransparent region in figure 10. We see that this region aligns well within 1σ with the green dotted contour.

There is another interesting difference between the ‘withBAO m ’ and the ‘noBAO $\alpha_{\parallel/\perp}$ ’ cases. The former only constrains the combination $\Omega_m h^2$ and is not able to disentangle the two parameters within the prior range. The latter, on the other hand, is able to distinguish between them and provides measurements on Ω_m and h of order $\sigma_{\Omega_m} \approx 0.08$ and $\sigma_h \approx 0.19$.

These constraints demonstrate that, in principle, the equality scale can be used as an uncalibrated standard ruler (see [34] and references therein) to measure the late-time expansion history, which is determined by Ω_m in the case of a flat- Λ CDM model. Still, the traditional BAO constraints (filled green contours) are tighter by factors 2 and 10 for Ω_m and h , respectively, which is a remarkable result and demonstrates the utility and robustness of the sound horizon as a standard ruler.

Because the power spectrum turnaround is at very large scales where cosmic variance is large, it is unlikely that this approach will be superior to the tried and tested BAO one. But there is a more severe problem with the k_{eq}^{-1} -based standard ruler approach. Cosmological constraints obtained from the calibrated equality scale measurement suffer a strong template-dependence. We visualize this issue in figure 11, where we explore the behavior of the relevant

‘withBAO’ and ‘noBAO’ cases when including (left panel) or not (right panel) the BBN-inspired prior on $\Omega_b h^2$.

The consequences of such prior for the ‘withBAO m -only’ case (magenta contours) are as follows. The power spectrum slope is now not only determined by $\Omega_m h^2$, but also by the baryon-to-cold-dark matter ratio, Ω_b/Ω_c . Hence, the cosmological fit shows a complete degeneracy between these two parameter combinations.

This evident degeneracy, however, is not at all captured in the ‘noBAO’ case (filled green contours), where $\Omega_m h$ seems overly well constrained in the case that the BBN prior is not included. Of course this is not surprising, since $k_{\text{eq}} \propto \Omega_m h$ does not depend on the baryon density $\Omega_b h^2$ (or ratio Ω_b/Ω_c) in any way. But since the fixed template fit at the previous compression step is carried out with a fixed $\Omega_b h^2$, the cosmological constraints from the so-obtained k_{eq} are not able to capture the correct degeneracies in cosmological parameter space. The *ShapeFit* parameterisation of the power spectrum shape through m , on the other hand, is flexible enough to capture a variety of models in a template-independent way.

We visualize this issue by carrying out additional fits using a template with an intentionally chosen displaced fiducial value for $\Omega_b^{\text{fid}} = 0.06$, deviating by 25% from the ‘true’ value $\Omega_b^{\text{true}} = 0.048$. Figure 11 demonstrates that, in the cases for which the template corresponds to $\Omega_b^{\text{fid}} = 0.06$, the m -derived cosmological constraints (black solid contours) do not deviate from the baseline results (magenta contours) by more than 1σ , whereas the k_{eq}^{-1} -derived constraints (black dotted contours) exhibit a clear shift (with respect to the green dashed lines) of 1.6σ in $\Omega_m h$ and 2.0σ in $\Omega_m h^2$ due to the incorrect value of Ω_b^{fid} in the template. This clearly demonstrates that calibrated k_{eq}^{-1} -based standard ruler methods would appear severely biased in case a wrong template is assumed. This could be remedied by either varying Ω_b at the stage of the template fit (and hence worsening the constraints) or adjusting the interpretation of $(\alpha_{\parallel}\alpha_{\perp}^2)^{1/3}$ towards $D_V k_{\text{eq}}$ by taking into account the baryon suppression consistently. We leave such an investigation for future work.

To summarize, we have shown that in theory it is possible to measure h by way of direct inferences of k_{eq}^{-1} as standard ruler, even for cosmologies with no sound horizon information at all (see the empty green dashed contour of figure 10). However there are a few reasons for scepticism. First, this h -measurements would not be competitive with respect to other methodologies and datasets (BAO, GW, SN, etc). Second, it is very hard to obtain such a measurement in a template-independent way using the standard methodology, as the one used for BAOofLSS. For that reason, previous works that have already tried to infer k_{eq}^{-1} -derived constraints on h , have employed model-dependent approaches, where the template shape varies at the same time as the cosmology inference (see for e.g., [36–38]). These measurements should not be interpreted as direct k_{eq}^{-1} -based standard ruler measurements though, but rather as measurements of h without the absolute value of the sound horizon (while still making use of the fact that the sound horizon is a standard ruler). Instead, their measurements are equivalent to our h_m measurement in section 4.

However, the (uncalibrated) k_{eq}^{-1} -based standard ruler analyses come with the prospect of delivering a sound horizon-independent Ω_m measurement. Obtained from the isotropic component ‘ D_V ’ -and hence relying on standard ruler property *ii*)-, this is also subject to some real-world subtleties as elaborated before. But if only the anisotropic ‘ F_{AP} ’ is used, which relies on assumption *i*), these issues can be remedied. In fact, in the work of [65] which includes a scaling of the broadband-only part of the power spectrum very similar to our treatment of the ‘noBAO’ mocks, they only use the anisotropic ‘ F_{AP} ’ part for cosmological interpretation for exactly the same reasons mentioned here. A promising research direction

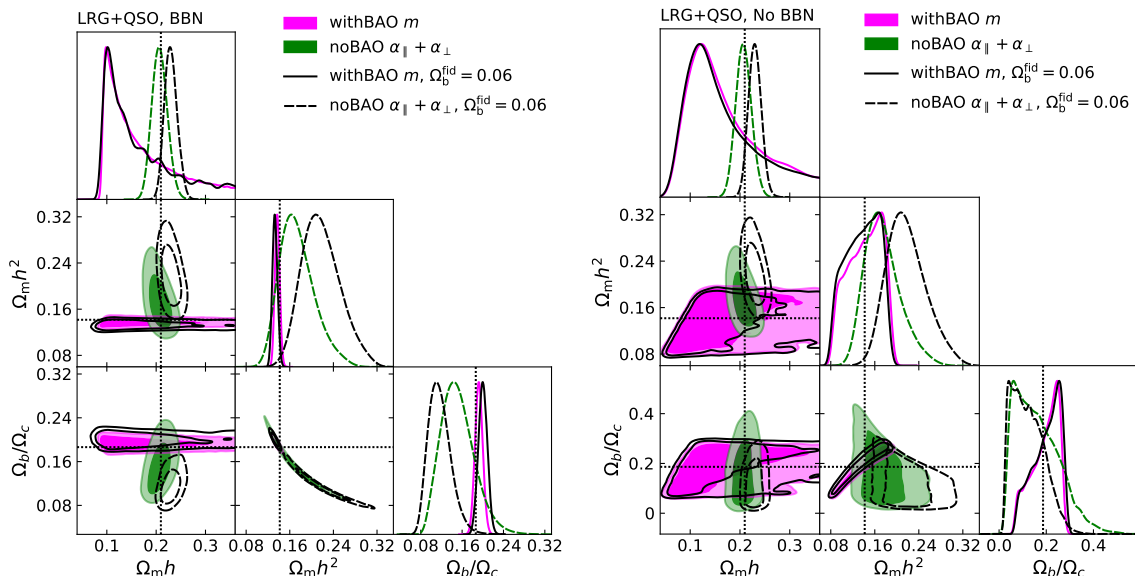


Figure 11. Impact of the choice of the fiducial value of Ω_b within the fixed-template fits, when employing k_{eq} as a ruler (green and dashed) or m as an anchor (magenta, solid black), with (left panel) or without (right panel) BBN prior during the cosmology inference. The results derived from a template-fit with a *correct* fiducial value for the baryon density, $\Omega_b = 0.048$, are shown in magenta contours (for the mocks with BAO, where only the shape parameter m is being used), and in green filled, dashed contours (for the mocks without BAO, using the scaling variables $\alpha_{\parallel, \perp}$ through eqs. (5.2)). Conversely, the cases where a *displaced* fiducial value for the baryon density is assumed for the shape of the template, $\Omega_b = 0.06$, are shown in black lines: solid for mocks with BAO when only considering the shape parameter m , and dashed for mocks without BAO when considering the scaling $\alpha_{\parallel, \perp}$ variables through eqs. (5.2). The true cosmology of the mocks is represented by the vertical and horizontal dotted lines. On one hand, the cosmology-derived contours from which k_{eq} is indirectly inferred from m (magenta bands and solid black lines for mocks with BAO) do not present any systematic shift with respect to the expected true values. On the other hand, the results derived from a direct inference of k_{eq} from the scaling $\alpha_{\parallel, \perp}$ variables (dashed lines) show a systematic offset when the value of Ω_b assumed on the fixed-template deviates from its true underlying value.

would hence be to combine their approach with our *ShapeFit* method, and as such enable a template-independent interpretation of the isotropic component as well. Since this is beyond the scope of this paper, we leave this for future research.

6 Discussion and conclusions

Direct, cosmic-distance ladder-based determinations of the Hubble parameter H_0 , anchored to $z \sim 0$ calibrators, are in tension with indirect determination of H_0 seen as a global parameter of the (extremely successful) standard Λ CDM model. Indirect determinations are usually anchored to early-time physics. This mismatch has motivated several proposed extensions to the Λ CDM model. A comprehensive analysis [18] clearly indicates that early-time solutions, models that involve new physics beyond Λ CDM model before recombination, are favored over late-time solutions.

The distance ladder-based H_0 determinations have several different anchors (Cepheids, TRGB, Masers, etc.), yet they mostly cluster around the high- H_0 ‘camp’. The early-time

physics determinations have one well-established and exquisitely determined anchor, the sound horizon at radiation drag. Within the standard Λ CDM model this quantity is determined by CMB observations with a $\sim 0.2\%$ error, it is, however, strongly model-dependent. It can also be determined independently of CMB observations e.g., [32, 33] by resorting to BBN, but it must still assume standard pre-recombination physics and a Λ CDM model or small parametric extensions to it. It is therefore of value to provide an independent early-time anchor for global indirect H_0 determinations.

This other anchor is provided by the physical processes at and around the matter-radiation equality era. We have shown that, in principle, the equality scale could be used as a standard(-izable) ruler, its signature being the turn-around of the matter power spectrum on large scales. This approach, however, at the moment is not really competitive. On the other hand the broadband shape of the matter power spectrum at large, linear scales is related to how fast modes re-entered the horizon at the end of the radiation era. We have shown how, under specific assumptions, the logarithmic slope of the power spectrum at those scales is related to how fast the horizon was expanding and can thus be seen as a “speedometer” at that epoch. This is a promising route to an equality-anchored H_0 determination.

We have performed such measurement using the *ShapeFit* approach and the state-of-the-art BOSS and eBOSS galaxy clustering data, finding the equality-anchored Hubble constant to be $H_0 = 70.1 \pm 2.1 \text{ km s}^{-1} \text{ Mpc}^{-1}$; this result represents the most precise measurement of H_0 to date, being independent of the sound horizon physics when LSS-only data (in combination of a BBN and a n_s priors) are used.

The modular and model-independent approach provided by *ShapeFit* enables us to perform a set of diagnostic tests where, for each relevant epoch or physical process, we assume that the Λ CDM model is a good effective model, but its parameters are not forced to be the same across all epochs and features (we call it piece-wise Λ CDM model). In this way we obtain two distinct H_0 ’s: the sound-horizon anchored, the equality anchored (and a third one which is the combination of the other two). We find broad agreement between the equality-anchored and the sound horizon-anchored H_0 ’s and this provides well defined guardrails for new physics beyond Λ CDM. To this aim, in table 2 we summarize our main results, clearly highlighting which physical assumptions are being made and which signatures (and combinations of signals) are being considered.

Early-time exotic models which aim to solve the Hubble tension via early-time modifications targeted to the sound-horizon scale, must account for matter-radiation equality effects, which in general would modify this other h too. For example, Early Dark Energy (EDE) models promise to reconcile the discrepancy between low- and high- H_0 values by invoking a phase of accelerated expansion shortly before recombination [39, 56, 84–88] and modifying the size of the sound-horizon ruler. In this way, when Λ CDM physics is assumed at pre-recombination times, the BAOofLSS measurements of H_0 would be incorrectly calibrated. EDE then must dissipate fast enough as to not affect the photon-diffusion scale and the angular scales that are tightly constrained by measurements of CMB anisotropies e.g., [62]. Naively, if this type of new physics leaves the matter-radiation equality physical processes almost unchanged, then (incorrectly) assuming a Λ CDM model throughout the data analysis would produce H_0 measurements derived from matter-radiation equality which may be in tension with the BAOofLSS H_0 measurements. We leave a detailed analysis of this specific case to future work.

Our results can be compared to previous works using an independent methodology to extract a sound horizon-free measurement of H_0 . In particular [38] reported $H_0 =$

Method	Λ CDM baseline model	Main Assumptions
$D_V/r_d + F_{\text{AP}}$ +BBN	$100 \times h_{r_d} = 67.42^{+0.88}_{-0.94}$	Late-time background expansion; Pre-recombination physics (standard r_d); $\Omega_m^{\text{early,r}} = \Omega_m^{\text{late}}$
$m + \mathfrak{D}_V + F_{\text{AP}}$ +BBN + n_s + $\sum m_\nu$	$100 \times h_m = 70.1 \pm 2.1$	Late-time background expansion; Equality physics; Standard r_d ; $\Omega_m^{\text{early,eq}} = \Omega_m^{\text{late}}$
$D_V/r_d + F_{\text{AP}}$ + m + BBN + $n_s + \sum m_\nu$	$100 \times h_{(m,r_d)} = 67.90^{+0.76}_{-0.75}$	Late-time background expansion; Equality physics; Pre-recombination physics (standard r_d); $\Omega_m^{\text{early,r}} = \Omega_m^{\text{early,eq}} = \Omega_m^{\text{late}}$
$\mathfrak{D}_V + F_{\text{AP}}$	$\Omega_m^{\text{late}} = 0.290^{+0.015}_{-0.016}$	Late-time background expansion; Standard r_d
m + BBN + $n_s + \sum m_\nu$	$[\Omega_m h^2]^{\text{early,eq}} = 0.1395 \pm 0.0036$	Equality physics

Table 2. Summary table displaying the most relevant results of this paper on h (3 first rows), and on Ω_m and $\Omega_m h^2$, in the last two rows, respectively, in all cases under the assumption of a flat Λ CDM model. The left column displays the set of compressed variables used within the datavector Θ (see eq. (3.1)), and also whether some priors are used on $\Omega_b h^2$ (see eq. (4.2) motivated by BBN), n_s (see eq. (4.3)) and $\sum m_\nu = 0.06 \text{ eV}$. The right column briefly summarize the physical assumptions that each set of variable makes. Finally, in the middle column we stress by the sub- or super-index whether this quantity is sensitive to early- or late-time physics, and whether is based on sound horizon scale’s (r_d), or matter-radiation equality epoch’s physics. (m or eq.).

$69.6^{+4.1}_{-5.4} \text{ km s}^{-1} \text{ Mpc}^{-1}$ using the BOSS LRGs data at $0.2 < z < 0.75$ ¹⁵. This can be compared to our LRG-only measurement (although we also include eBOSS LRGs, thus $0.2 < z < 1.0$) of $H_0 = 64.5^{+3.5}_{-4.5} \text{ km s}^{-1} \text{ Mpc}^{-1}$; and $H_0 = 70.2^{+1.9}_{-2.1} \text{ km s}^{-1} \text{ Mpc}^{-1}$ for LRG+QSO+Lyman- α in the full range of $0.2 < z < 3.5$. Consistently using all BOSS and eBOSS data shrinks the errorbars by a factor of ~ 2 compared to previous results. Even when using only the LRG galaxies, our results is notably tighter, possibly because of the high- z eBOSS galaxies and BAO reconstruction, which significantly help to determine the Ω_m value through the uncalibrated BAO (Table 3). Part of the difference in error bar can also be explained by the slightly different prior choices for cosmological parameters with respect to [38]. If we match their setup, we obtain $H_0 = 65.5^{+3.9}_{-4.6} \text{ km s}^{-1} \text{ Mpc}^{-1}$ for the LRG Sample only.

The H_0 tension is truly a tale of two h : the local (direct, late-Universe) and the global (indirect). There are in reality (many) more than two ways, independent and based on very different physics, to measure H_0 ; yet, they all cluster around the early/low and late/high camps. Importantly, the two H_0 determinations presented here, anchored at early times and based on different early-Universe physics ingredients, are consistent with each other. The newer determination, independent of CMB observations and independent of the sound horizon and anchored at equality, has now competitive error bars, $\sim 3\%$; whereas the sound horizon-based one, also independent of CMB observations, has a 1.5% error. We envision

¹⁵We choose this value among other values reported in their analysis to be the closest to our analysis setup which relies on minimum assumptions based on external datasets to BOSS. In particular for this value they choose a BBN prior, a neutrino mass sum bound of $\sum m_\nu < 0.26 \text{ eV}$ and a spectral index prior of $n_s = 0.96 \pm 0.02$, and assuming a flat- $\nu\Lambda$ CDM model.

that forthcoming improvements on these large-scale structure-based measurements will act as guardrails on the road to a solution to this persistent tension.

Acknowledgments

We thank Nils Schöneberg, José Luis Bernal, Adam Riess and Tristan Smith for useful comments on an advanced version of this manuscript. We also thank the anonymous referee for their constructive feedback that helped improve the manuscript. For the purpose of open access, the author has applied a Creative Commons Attribution (CC BY) licence to any Author Accepted Manuscript version arising from this submission. SB acknowledges support from the European Research Council (ERC) under the European Union’s Horizon 2020 research and innovation program (FutureLSS, grant agreement 853291). HGM and LV acknowledge support of European Union’s Horizon 2020 research and innovation programme ERC (BePreSySe, grant agreement 725327).

Funding for this work was partially provided by the Spanish MINECO under project PGC2018-098866-B-I00MCIN/AEI/10.13039/501100011033 y FEDER “Una manera de hacer Europa”, and the “Center of Excellence Maria de Maeztu 2020-2023” award to the ICCUB (CEX2019-000918-M funded by MCIN/AEI/10.13039/501100011033). We acknowledge the IT team at ICCUB for the help with the AGANICE cluster where all the calculations presented in this paper were done.

A The impact of priors on $\Omega_b h^2$ and n_s

We explore the effects of some of the assumptions made in our baseline analysis. First, we investigate the impact of excluding the prior on $\Omega_b h^2$ motivated by BBN observations. Second, we evaluate the impact of fixing $n_s = 0.97$ in our baseline analysis versus allowing n_s to vary within a Gaussian prior specified below.

The effect of removing the BBN priors on $\Omega_b h^2$ is displayed in the left panel of figure 12, where the dashed (solid) lines represent the BBN prior (flat prior $[0.1 < 100\Omega_b h^2 < 4.0]$) results on the Λ CDM parameters for the different variable combinations using geometry, shape and growth, as described in the legend, and using the same colour notation as in figures 5,6. On the one hand, the $\Omega_b h^2$ prior has no effect on Ω_m and σ_8 . Ω_m is essentially constrained from the uncalibrated BAO signal, which depends on relative $D_V(z_i)/r_d$ measurements at different redshifts (noted as $\mathfrak{D}_V(z_i)$ when r_d is marginalized over), and by the Alcock-Paczynski parameter, F_{AP} , both fully independent of r_d , and therefore of $\Omega_b h^2$. The σ_8 parameter is inferred from the redshift-space variable $f\sigma_{s8}$ once Ω_m is known (from the uncalibrated BAO) and GR is assumed (for the $f \sim \Omega_m^{0.56}$ relation), again fully independent of $\Omega_b h^2$. On the other hand, the results on h are highly affected by the $\Omega_b h^2$ prior. On the sound horizon-calibrated results (cyan lines), the $\Omega_b h^2$ measurement is key to determine the absolute size of r_d (once the early-time Λ CDM physics are assumed) and therefore determine h . For results obtained via the shape variable m (red lines), $\Omega_b h^2$ plays a key role on determining the baryon suppression in the transfer function with sufficient precision to establish a connection between matter-radiation equality and the slope, and thus determine h .

Even when combining the BBN-free results taking the full D_V/r_d and shape, m , information, h remains undetermined (dashed blue lines), although the effects of $\Omega_b h^2$ on r_d on one hand and on the shape on the other hand are of very different nature. It appears that the physical CDM density $\Omega_c h^2$ is able to compensate for both effects in parallel while still fitting

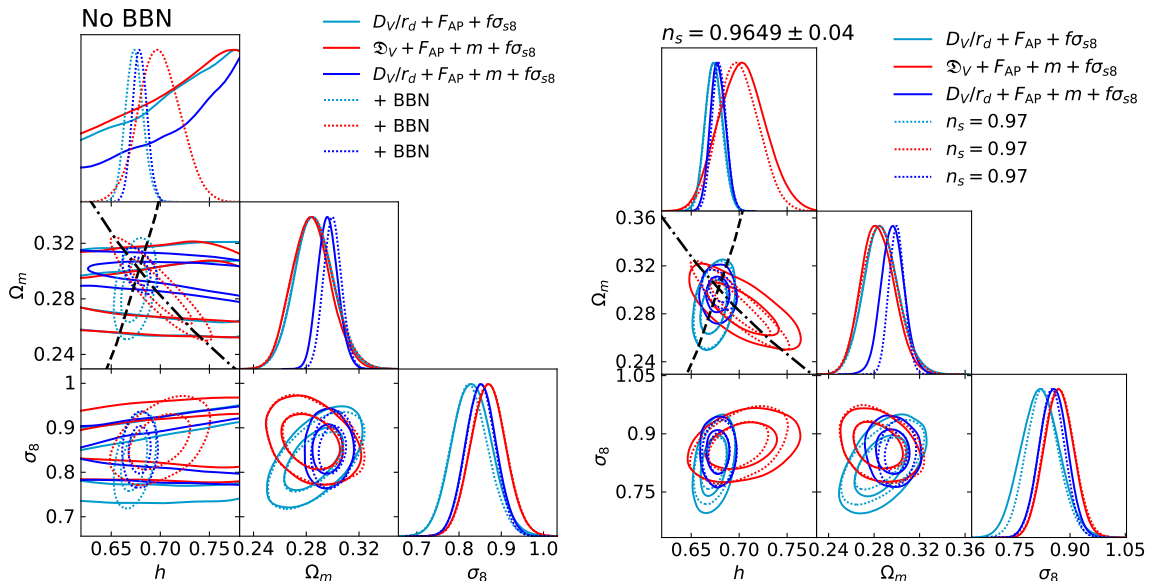


Figure 12. Left panel: effect of removing the BBN prior on $\Omega_b h^2$ in the parameters of a flat Λ CDM model, for the geometry+shape+growth case. The dotted lines display the most relevant cases of figure 5 (i.e., with the BBN prior on $\Omega_b h^2$), whereas the solid lines represent the effect of setting a wide and uninformative uniform prior on $\Omega_b h^2$. As expected, Ω_m is unaffected by the prior, as its constraints come from the relative BAO peak positions in different directions and at different redshifts ($\mathfrak{D}_V + F_{AP}$ case); similarly σ_8 is also unaffected as it is constrained by the redshift space distortions, i.e., the relative amplitudes of the isotropic and anisotropic signals, mainly at large scales. Only h is significantly affected: 1) a free $\Omega_b h^2$ de-calibrates the horizon scale ruler size, which can take almost any value; 2) a free $\Omega_b h^2$ also washes out the information on $\Omega_m h^2$ from the shape, because of a ‘free’ baryon suppression. As a consequence, without a precise $\Omega_b h^2$ constraint the system loses its ‘two anchors’ and only Ω_m and σ_8 can be efficiently determined. Right panel: effect of considering a Gaussian prior on n_s centered around the Planck best-fit value $n_s = 0.9649 \pm 0.04$ where the width corresponds to 10- σ Planck sensitivity versus fixing $n_s = 0.97$ in our baseline setup. As expected, this leads to a broadening of the shape-derived constraints (red) on h , while the sound-horizon based constraint (cyan) is essentially unaffected. The Ω_m constraints are completely unaffected, but there is a mild increase in error on σ_8 .

the *ShapeFit* data. In order to break this degeneracy we would require additional information related to $\Omega_b h^2$, for example the amplitude of the BAO peak, although it is not clear whether this would appreciably tighten our constraints in the case without BBN. We leave such an investigation for future work.

In the right panel of figure 12 we show the impact of employing a Gaussian prior on the spectral index $n_s = 0.9649 \pm 0.04$ instead of fixing it to $n_s = 0.97$ as in our baseline analysis. The prior width represents 10- σ deviations given the Planck sensitivity [9]. We can see that the impact of such a prior is mild. The error on σ_8 slightly increases (by 20%) in the geometry+growth (cyan) case. The constraint on h on the other hand barely changes in that case. Only upon including the shape m , varying n_s appreciably changes the constraints. In particular, it inflates the $\Omega_m - h$ degeneracy in the sound horizon-independent case (red), such that our fixed n_s constraint $H_0 = 70.2_{-2.1}^{+1.9} \text{ km s}^{-1} \text{ Mpc}^{-1}$ changes to $H_0 = 70.4_{-2.8}^{+2.2} \text{ km s}^{-1} \text{ Mpc}^{-1}$ once we relax that assumption. As a consequence, the combined constraint (blue) mildly changes from $H_0 = 67.90_{-0.75}^{+0.76} \text{ km s}^{-1} \text{ Mpc}^{-1}$ to $H_0 = 67.80_{-0.84}^{+0.78} \text{ km s}^{-1} \text{ Mpc}^{-1}$, being still

remarkably competitive with respect to the local distance determination [69]. In parallel, the combined constraint on the matter density also changes from $\Omega_m = 0.3000^{+0.0065}_{-0.0073}$ to $\Omega_m = 0.2963^{+0.0096}_{-0.011}$, as an effect of the inflated $\Omega_m - h$ degeneracy mentioned earlier. But note that this only affects the Ω_m^{early} part coming from the shape. The Ω_m^{late} part from geometry is not influenced by varying n_s at all.

B Summary of all cosmological constraints

Table 3 displays the full results for different combinations presented in the paper, for the full LRG+QSO+Lyman- α full redshift range, $0.2 < z < 3.5$. Note that there are small differences in the error bar with respect to equivalent cases reported in table 9 of [21]. This is because the transformation of the $(D_M/r_d, D_H/r_d)$ towards the $(D_V/r_d, F_{\text{AP}})$ basis induces small numerical fluctuations.

Model	Case	$H_0[\text{km s}^{-1}\text{Mpc}^{-1}]$	Ω_m	σ_8
ΛCDM	$F_{\text{AP}} + m$	$69.5^{+4.2}_{-5.1}$	$0.292^{+0.034}_{-0.041}$	-
ΛCDM	$\mathcal{D}_V + F_{\text{AP}} + m$	$70.1^{+2.1}_{-2.1}$	$0.286^{+0.013}_{-0.017}$	-
ΛCDM	$D_V/r_d + F_{\text{AP}}$	$67.42^{+0.88}_{-0.94}$	$0.290^{+0.015}_{-0.016}$	-
ΛCDM	$D_V/r_d + F_{\text{AP}} + m$	$67.90^{+0.76}_{-0.75}$	$0.3019^{+0.0074}_{-0.0069}$	-
ΛCDM	$F_{\text{AP}} + m + f\sigma_{s8}$	$72.8^{+4.0}_{-4.8}$	$0.264^{+0.029}_{-0.033}$	$0.897^{+0.047}_{-0.055}$
ΛCDM	$\mathcal{D}_V + F_{\text{AP}} + m + f\sigma_{s8}$	$70.2^{+1.9}_{-2.1}$	$0.284^{+0.014}_{-0.016}$	$0.872^{+0.042}_{-0.042}$
ΛCDM	$D_V/r_d + F_{\text{AP}} + f\sigma_{s8}$	$67.37^{+0.86}_{-0.95}$	$0.286^{+0.014}_{-0.016}$	$0.825^{+0.043}_{-0.047}$
ΛCDM	$D_V/r_d + F_{\text{AP}} + m + f\sigma_{s8}$	$67.90^{+0.76}_{-0.75}$	$0.3000^{+0.0065}_{-0.0073}$	$0.850^{+0.035}_{-0.038}$
ΛCDM (free n_s)	$F_{\text{AP}} + m + f\sigma_{s8}$	$73.0^{+4.6}_{-4.7}$	$0.265^{+0.027}_{-0.034}$	$0.894^{+0.051}_{-0.052}$
ΛCDM (free n_s)	$\mathcal{D}_V + F_{\text{AP}} + m + f\sigma_{s8}$	$70.4^{+2.2}_{-2.8}$	$0.283^{+0.014}_{-0.016}$	$0.870^{+0.042}_{-0.042}$
ΛCDM (free n_s)	$D_V/r_d + F_{\text{AP}} + f\sigma_{s8}$	$67.36^{+0.92}_{-0.94}$	$0.286^{+0.014}_{-0.016}$	$0.820^{+0.052}_{-0.055}$
ΛCDM (free n_s)	$D_V/r_d + F_{\text{AP}} + m + f\sigma_{s8}$	$67.80^{+0.78}_{-0.84}$	$0.2963^{+0.0096}_{-0.011}$	$0.855^{+0.037}_{-0.039}$
ΛCDM (no-BBN)	$F_{\text{AP}} + m + f\sigma_{s8}$	-	$0.264^{+0.028}_{-0.033}$	$0.892^{+0.048}_{-0.055}$
ΛCDM (no-BBN)	$\mathcal{D}_V + F_{\text{AP}} + m + f\sigma_{s8}$	-	$0.284^{+0.014}_{-0.016}$	$0.869^{+0.040}_{-0.043}$
ΛCDM (no-BBN)	$D_V/r_d + F_{\text{AP}} + f\sigma_{s8}$	-	$0.286^{+0.014}_{-0.016}$	$0.831^{+0.046}_{-0.048}$
ΛCDM (no-BBN)	$D_V/r_d + F_{\text{AP}} + m + f\sigma_{s8}$	-	$0.2964^{+0.0073}_{-0.0083}$	$0.852^{+0.036}_{-0.038}$
$\nu\Lambda\text{CDM}$	$F_{\text{AP}} + m + f\sigma_{s8}$	$76.2^{+5.0}_{-5.5}$	$0.265^{+0.029}_{-0.035}$	$0.935^{+0.054}_{-0.065}$
$\nu\Lambda\text{CDM}$	$\mathcal{D}_V + F_{\text{AP}} + m + f\sigma_{s8}$	$73.3^{+3.0}_{-3.3}$	$0.284^{+0.014}_{-0.015}$	$0.906^{+0.048}_{-0.050}$
$\nu\Lambda\text{CDM}$	$D_V/r_d + F_{\text{AP}} + f\sigma_{s8}$	$66.35^{+1.1}_{-1.2}$	$0.287^{+0.015}_{-0.016}$	$0.786^{+0.054}_{-0.054}$
$\nu\Lambda\text{CDM}$	$D_V/r_d + F_{\text{AP}} + m + f\sigma_{s8}$	$67.86^{+0.78}_{-0.74}$	$0.304^{+0.008}_{-0.011}$	$0.853^{+0.035}_{-0.036}$
$N_{\text{eff}}\Lambda\text{CDM}$	$F_{\text{AP}} + m + f\sigma_{s8}$	$68.8^{+3.2}_{-3.3}$	$0.291^{+0.024}_{-0.025}$	$0.866^{+0.041}_{-0.044}$
$N_{\text{eff}}\Lambda\text{CDM}$	$\mathcal{D}_V + F_{\text{AP}} + m + f\sigma_{s8}$	$69.9^{+2.5}_{-2.5}$	$0.283^{+0.014}_{-0.016}$	$0.870^{+0.039}_{-0.044}$
$N_{\text{eff}}\Lambda\text{CDM}$	$D_V/r_d + F_{\text{AP}} + f\sigma_{s8}$	$66.66^{+2.1}_{-2.1}$	$0.286^{+0.014}_{-0.015}$	$0.822^{+0.045}_{-0.046}$
$N_{\text{eff}}\Lambda\text{CDM}$	$D_V/r_d + F_{\text{AP}} + m + f\sigma_{s8}$	$67.90^{+1.9}_{-1.9}$	$0.2999^{+0.0075}_{-0.0087}$	$0.850^{+0.036}_{-0.035}$

Table 3. Results on $H_0 = 100h[\text{km s}^{-1}\text{Mpc}^{-1}]$, Ω_m and σ_8 when employing the full set of LRG+QSO+Lyman- α BOSS and eBOSS data in the range $0.2 < z < 3.5$. Different rows show different assumptions on the underlying model (first column) and different combination of compressed variables (second column, see section 4 for notation). These results show the cases displayed in figure 4-6.

References

- [1] B. Abareschi, J. Aguilar, S. Ahlen, S. Alam, D.M. Alexander, R. Alfarsy et al., *Overview of the Instrumentation for the Dark Energy Spectroscopic Instrument*, *AJ* **164** (2022) 207 [2205.10939].
- [2] R. Laureijs, J. Amiaux, S. Arduini, J.L. Auguères, J. Brinchmann, R. Cole et al., *Euclid Definition Study Report*, *arXiv e-prints* (2011) arXiv:1110.3193 [1110.3193].
- [3] Ž. Ivezić, S.M. Kahn, J.A. Tyson, B. Abel, E. Acosta, R. Allsman et al., *LSST: From Science Drivers to Reference Design and Anticipated Data Products*, *ApJ* **873** (2019) 111 [0805.2366].
- [4] D. Spergel, N. Gehrels, C. Baltay, D. Bennett, J. Breckinridge, M. Donahue et al., *Wide-Field Infrared Survey Telescope-Astrophysics Focused Telescope Assets WFIRST-AFTA 2015 Report*, *arXiv e-prints* (2015) arXiv:1503.03757 [1503.03757].
- [5] SKA collaboration, *Cosmology with Phase 1 of the Square Kilometre Array: Red Book 2018: Technical specifications and performance forecasts*, *Publ. Astron. Soc. Austral.* **37** (2020) e007 [1811.02743].
- [6] P. Ade, J. Aguirre, Z. Ahmed, S. Aiola, A. Ali, D. Alonso et al., *The Simons Observatory: science goals and forecasts*, *J. Cosmology Astropart. Phys.* **2019** (2019) 056 [1808.07445].
- [7] A.G. Riess et al., *A Comprehensive Measurement of the Local Value of the Hubble Constant with 1 km/s/Mpc Uncertainty from the Hubble Space Telescope and the SH0ES Team*, *Astrophys. J. Lett.* **934** (2022) L7 [2112.04510].
- [8] L. Verde, T. Treu and A.G. Riess, *Tensions between the early and late Universe*, *Nature Astronomy* **3** (2019) 891 [1907.10625].
- [9] Planck Collaboration, N. Aghanim, Y. Akrami, M. Ashdown, J. Aumont, C. Baccigalupi et al., *Planck 2018 results. VI. Cosmological parameters*, *A&A* **641** (2020) A6 [1807.06209].
- [10] W.L. Freedman, B.F. Madore, T. Hoyt, I.S. Jang, R. Beaton, M.G. Lee et al., *Calibration of the Tip of the Red Giant Branch*, *ApJ* **891** (2020) 57 [2002.01550].
- [11] K.C. Wong, S.H. Suyu, G.C.F. Chen, C.E. Rusu, M. Millon, D. Sluse et al., *H0LiCOW - XIII. A 2.4 per cent measurement of H_0 from lensed quasars: 5.3 σ tension between early- and late-Universe probes*, *MNRAS* **498** (2020) 1420 [1907.04869].
- [12] S. Alam, F.D. Albareti, C. Allende Prieto, F. Anders, S.F. Anderson, T. Anderton et al., *The Eleventh and Twelfth Data Releases of the Sloan Digital Sky Survey: Final Data from SDSS-III*, *ApJS* **219** (2015) 12 [1501.00963].
- [13] S. Alam, M. Aubert, S. Avila, C. Balland, J.E. Bautista, M.A. Bershadsky et al., *Completed SDSS-IV extended Baryon Oscillation Spectroscopic Survey: Cosmological implications from two decades of spectroscopic surveys at the Apache Point Observatory*, *Phys. Rev. D* **103** (2021) 083533 [2007.08991].
- [14] C. Blake, S. Brough, M. Colless, C. Contreras, W. Couch, S. Croom et al., *The WiggleZ Dark Energy Survey: joint measurements of the expansion and growth history at $z < 1$* , *MNRAS* **425** (2012) 405 [1204.3674].
- [15] E. Di Valentino, O. Mena, S. Pan, L. Visinelli, W. Yang, A. Melchiorri et al., *In the realm of the Hubble tension—a review of solutions*, *Class. Quant. Grav.* **38** (2021) 153001 [2103.01183].
- [16] A.J. Cuesta, L. Verde, A. Riess and R. Jimenez, *Calibrating the cosmic distance scale ladder: the role of the sound-horizon scale and the local expansion rate as distance anchors*, *MNRAS* **448** (2015) 3463 [1411.1094].
- [17] É. Aubourg, S. Bailey, J.E. Bautista, F. Beutler, V. Bhardwaj, D. Bizyaev et al., *Cosmological implications of baryon acoustic oscillation measurements*, *Phys. Rev. D* **92** (2015) 123516 [1411.1074].

- [18] N. Schöneberg, G.F. Abellán, A.P. Sánchez, S.J. Witte, V. Poulin and J. Lesgourgues, *The H_0 Olympics: A fair ranking of proposed models*, *Phys. Rep.* **984** (2022) 1 [2107.10291].
- [19] M. Kamionkowski and A.G. Riess, *The Hubble Tension and Early Dark Energy*, *arXiv e-prints* (2022) arXiv:2211.04492 [2211.04492].
- [20] S. Brieden, H. Gil-Marín and L. Verde, *ShapeFit: extracting the power spectrum shape information in galaxy surveys beyond BAO and RSD*, *J. Cosmology Astropart. Phys.* **2021** (2021) 054 [2106.07641].
- [21] S. Brieden, H. Gil-Marín and L. Verde, *Model-agnostic interpretation of 10 billion years of cosmic evolution traced by BOSS and eBOSS data*, *J. Cosmology Astropart. Phys.* **2022** (2022) 024 [2204.11868].
- [22] S. Brieden, H. Gil-Marín and L. Verde, “BOSS and eBOSS data-vectors and covariances for SHAPEFIT.” https://www.ub.edu/bispectrum/sdss_shapefit.html.
- [23] M. Tegmark, M.R. Blanton, M.A. Strauss, F. Hoyle, D. Schlegel, R. Scoccimarro et al., *The Three-Dimensional Power Spectrum of Galaxies from the Sloan Digital Sky Survey*, *ApJ* **606** (2004) 702 [astro-ph/0310725].
- [24] G. d’Amico, J. Gleyzes, N. Kokron, K. Markovic, L. Senatore, P. Zhang et al., *The cosmological analysis of the SDSS/BOSS data from the Effective Field Theory of Large-Scale Structure*, *J. Cosmology Astropart. Phys.* **2020** (2020) 005 [1909.05271].
- [25] M.M. Ivanov, M. Simonović and M. Zaldarriaga, *Cosmological parameters from the BOSS galaxy power spectrum*, *J. Cosmology Astropart. Phys.* **2020** (2020) 042 [1909.05277].
- [26] T. Tröster, A.G. Sánchez, M. Asgari, C. Blake, M. Crocce, C. Heymans et al., *Cosmology from large-scale structure. Constraining Λ CDM with BOSS*, *A&A* **633** (2020) L10 [1909.11006].
- [27] J. Hamann, S. Hannestad, J. Lesgourgues, C. Rampf and Y.Y.Y. Wong, *Cosmological parameters from large scale structure - geometric versus shape information*, *J. Cosmology Astropart. Phys.* **2010** (2010) 022 [1003.3999].
- [28] O. Pisanti, A. Cirillo, S. Esposito, F. Iocco, G. Mangano, G. Miele et al., *PARthENoPE: Public Algorithm Evaluating the Nucleosynthesis of Primordial Elements*, *Comput. Phys. Commun.* **178** (2008) 956 [0705.0290].
- [29] E.G. Adelberger et al., *Solar fusion cross sections II: the pp chain and CNO cycles*, *Rev. Mod. Phys.* **83** (2011) 195 [1004.2318].
- [30] G.E. Addison, D.J. Watts, C.L. Bennett, M. Halpern, G. Hinshaw and J.L. Weiland, *Elucidating Λ CDM: Impact of Baryon Acoustic Oscillation Measurements on the Hubble Constant Discrepancy*, *ApJ* **853** (2018) 119 [1707.06547].
- [31] A. Cuceu, J. Farr, P. Lemos and A. Font-Ribera, *Baryon Acoustic Oscillations and the Hubble constant: past, present and future*, *J. Cosmology Astropart. Phys.* **2019** (2019) 044 [1906.11628].
- [32] N. Schöneberg, J. Lesgourgues and D.C. Hooper, *The BAO+BBN take on the Hubble tension*, *JCAP* **10** (2019) 029 [1907.11594].
- [33] N. Schöneberg, L. Verde, H. Gil-Marín and S. Brieden, *BAO+BBN revisited - growing the Hubble tension with a 0.7 km/s/Mpc constraint*, *J. Cosmology Astropart. Phys.* **2022** (2022) 039 [2209.14330].
- [34] S. Cunnington, *Detecting the power spectrum turnover with H I intensity mapping*, *MNRAS* **512** (2022) 2408 [2202.13828].
- [35] C. Blake and S. Bridle, *Cosmology with photometric redshift surveys*, *MNRAS* **363** (2005) 1329 [astro-ph/0411713].

- [36] O.H.E. Philcox, B.D. Sherwin, G.S. Farren and E.J. Baxter, *Determining the Hubble constant without the sound horizon: Measurements from galaxy surveys*, *Phys. Rev. D* **103** (2021) 023538 [2008.08084].
- [37] G.S. Farren, O.H.E. Philcox and B.D. Sherwin, *Determining the Hubble constant without the sound horizon: Perspectives with future galaxy surveys*, *Phys. Rev. D* **105** (2022) 063503 [2112.10749].
- [38] O.H.E. Philcox, G.S. Farren, B.D. Sherwin, E.J. Baxter and D.J. Brout, *Determining the Hubble constant without the sound horizon: A 3.6 % constraint on H_0 from galaxy surveys, CMB lensing, and supernovae*, *Phys. Rev. D* **106** (2022) 063530 [2204.02984].
- [39] T.L. Smith, V. Poulin and T. Simon, *Assessing the robustness of sound horizon-free determinations of the Hubble constant*, 2208.12992.
- [40] A. Amon and G. Efstathiou, *A non-linear solution to the S_8 tension?*, *MNRAS* **516** (2022) 5355 [2206.11794].
- [41] R. Maartens, *Is the Universe homogeneous?*, *Phil. Trans. Roy. Soc. Lond. A* **369** (2011) 5115 [1104.1300].
- [42] D. Blas, M. Garny, M.M. Ivanov and S. Sibiryakov, *Time-sliced perturbation theory II: baryon acoustic oscillations and infrared resummation*, *J. Cosmology Astropart. Phys.* **2016** (2016) 028 [1605.02149].
- [43] D.J. Eisenstein, H.-J. Seo, E. Sirko and D.N. Spergel, *Improving Cosmological Distance Measurements by Reconstruction of the Baryon Acoustic Peak*, *ApJ* **664** (2007) 675 [astro-ph/0604362].
- [44] A. Burden, W.J. Percival and C. Howlett, *Reconstruction in Fourier space*, *Monthly Notices of the Royal Astronomical Society* **453** (2015) 456 [1504.02591].
- [45] B.D. Sherwin and M. White, *The impact of wrong assumptions in BAO reconstruction*, *Journal of Cosmology and Astroparticle Physics* **2019** (2019) 027 [1808.04384].
- [46] J. Blazek, J.E. McEwen and C.M. Hirata, *Streaming velocities and the baryon-acoustic oscillation scale*, *Phys. Rev. Lett.* **116** (2016) 121303 [1510.03554].
- [47] Z. Slepian et al., *Constraining the baryon–dark matter relative velocity with the large-scale three-point correlation function of the SDSS BOSS DR12 CMASS galaxies*, *Mon. Not. Roy. Astron. Soc.* **474** (2018) 2109 [1607.06098].
- [48] C.M. Hirata, *Small-scale structure and the Lyman- α forest baryon acoustic oscillation feature*, *Mon. Not. Roy. Astron. Soc.* **474** (2018) 2173 [1707.03358].
- [49] T. Nishimichi, G. D’Amico, M.M. Ivanov, L. Senatore, M. Simonović, M. Takada et al., *Blinded challenge for precision cosmology with large-scale structure: results from effective field theory for the redshift-space galaxy power spectrum*, *Phys. Rev. D* **102** (2020) 123541 [2003.08277].
- [50] T. Nishimichi, “Multipole moment data for PT challenges.” <https://www2.yukawa.kyoto-u.ac.jp/~takahiro.nishimichi/data/PTchallenge/>.
- [51] S. Brieden, H. Gil-Marín and L. Verde, *PT challenge: validation of ShapeFit on large-volume, high-resolution mocks*, *J. Cosmology Astropart. Phys.* **2022** (2022) 005 [2201.08400].
- [52] B. Reid, S. Ho, N. Padmanabhan, W.J. Percival, J. Tinker, R. Tojeiro et al., *SDSS-III Baryon Oscillation Spectroscopic Survey Data Release 12: galaxy target selection and large-scale structure catalogues*, *MNRAS* **455** (2016) 1553 [1509.06529].
- [53] A.J. Ross, J. Bautista, R. Tojeiro, S. Alam, S. Bailey, E. Burtin et al., *The Completed SDSS-IV extended Baryon Oscillation Spectroscopic Survey: Large-scale structure catalogues for cosmological analysis*, *MNRAS* **498** (2020) 2354 [2007.09000].

- [54] B.W. Lyke, A.N. Higley, J.N. McLane, D.P. Schurhammer, A.D. Myers, A.J. Ross et al., *The Sloan Digital Sky Survey Quasar Catalog: Sixteenth Data Release*, *ApJS* **250** (2020) 8 [2007.09001].
- [55] S. Brieden, H. Gil-Marín and L. Verde, *Model-independent versus model-dependent interpretation of the SDSS-III BOSS power spectrum: Bridging the divide*, *Phys. Rev. D* **104** (2021) L121301 [2106.11931].
- [56] T. Simon, P. Zhang, V. Poulin and T.L. Smith, *On the consistency of effective field theory analyses of BOSS power spectrum*, 2208.05929.
- [57] S.-F. Chen, Z. Vlah and M. White, *A new analysis of galaxy 2-point functions in the BOSS survey, including full-shape information and post-reconstruction BAO*, *J. Cosmology Astropart. Phys.* **2022** (2022) 008 [2110.05530].
- [58] J.L. Bernal, L. Verde and A.G. Riess, *The trouble with H_0* , *Journal of Cosmology and Astro-Particle Physics* **10** (2016) 019 [1607.05617].
- [59] A. Heavens, R. Jimenez and L. Verde, *Standard Rulers, Candles, and Clocks from the Low-Redshift Universe*, *Phys. Rev. Lett.* **113** (2014) 241302 [1409.6217].
- [60] L. Verde, J.L. Bernal, A.F. Heavens and R. Jimenez, *The length of the low-redshift standard ruler*, *MNRAS* **467** (2017) 731 [1607.05297].
- [61] É. Aubourg, S. Bailey, J.E. Bautista, F. Beutler, V. Bhardwaj, D. Bizyaev et al., *Cosmological implications of baryon acoustic oscillation measurements*, *Phys. Rev. D* **92** (2015) 123516 [1411.1074].
- [62] L. Knox and M. Millea, *Hubble constant hunter’s guide*, *Phys. Rev. D* **101** (2020) 043533 [1908.03663].
- [63] SPT-3G collaboration, *Measurements of the E-mode polarization and temperature-E-mode correlation of the CMB from SPT-3G 2018 data*, *Phys. Rev. D* **104** (2021) 022003 [2101.01684].
- [64] ACT collaboration, *The Atacama Cosmology Telescope: DR4 Maps and Cosmological Parameters*, *JCAP* **12** (2020) 047 [2007.07288].
- [65] A. Cuceu, A. Font-Ribera, B. Joachimi and S. Nadathur, *Cosmology beyond BAO from the 3D distribution of the Lyman- α forest*, *Mon. Not. Roy. Astron. Soc.* **506** (2021) 5439 [2103.14075].
- [66] D. Scolnic, D. Brout, A. Carr, A.G. Riess, T.M. Davis, A. Dwomoh et al., *The Pantheon+ Analysis: The Full Data Set and Light-curve Release*, *ApJ* **938** (2022) 113 [2112.03863].
- [67] D. Brout, D. Scolnic, B. Popovic, A.G. Riess, A. Carr, J. Zuntz et al., *The Pantheon+ Analysis: Cosmological Constraints*, *ApJ* **938** (2022) 110 [2202.04077].
- [68] A.G. Riess, *The expansion of the Universe is faster than expected*, *Nature Reviews Physics* **2** (2020) 10 [2001.03624].
- [69] A.G. Riess, W. Yuan, L.M. Macri, D. Scolnic, D. Brout, S. Casertano et al., *A Comprehensive Measurement of the Local Value of the Hubble Constant with $1 \text{ km s}^{-1} \text{ Mpc}^{-1}$ Uncertainty from the Hubble Space Telescope and the SH0ES Team*, *ApJ* **934** (2022) L7 [2112.04510].
- [70] J.L. Bernal, L. Verde, R. Jimenez, M. Kamionkowski, D. Valcin and B.D. Wandelt, *Trouble beyond H_0 and the new cosmic triangles*, *Phys. Rev. D* **103** (2021) 103533 [2102.05066].
- [71] J. Hou, A.G. Sánchez, A.J. Ross, A. Smith, R. Neveux, J. Bautista et al., *The completed SDSS-IV extended Baryon Oscillation Spectroscopic Survey: BAO and RSD measurements from anisotropic clustering analysis of the quasar sample in configuration space between redshift 0.8 and 2.2*, *MNRAS* **500** (2021) 1201 [2007.08998].
- [72] R. Neveux, E. Burtin, A. de Mattia, A. Smith, A.J. Ross, J. Hou et al., *The completed SDSS-IV extended Baryon Oscillation Spectroscopic Survey: BAO and RSD measurements*

from the anisotropic power spectrum of the quasar sample between redshift 0.8 and 2.2, *MNRAS* **499** (2020) 210 [2007.08999].

- [73] H. du Mas des Bourboux et al., *The Completed SDSS-IV Extended Baryon Oscillation Spectroscopic Survey: Baryon Acoustic Oscillations with Ly α Forests*, *Astrophys. J.* **901** (2020) 153 [2007.08995].
- [74] R.J. Cooke, M. Pettini and C.C. Steidel, *One Percent Determination of the Primordial Deuterium Abundance*, *ApJ* **855** (2018) 102 [1710.11129].
- [75] D. Blas, J. Lesgourgues and T. Tram, *The Cosmic Linear Anisotropy Solving System (CLASS). Part II: Approximation schemes*, *Journal of Cosmology and Astro-Particle Physics* **2011** (2011) 034 [1104.2933].
- [76] T. Brinckmann and J. Lesgourgues, *MontePython 3: boosted MCMC sampler and other features*, *Phys. Dark Univ.* **24** (2019) 100260 [1804.07261].
- [77] H. Gil-Marín, W.J. Percival, L. Verde, J.R. Brownstein, C.-H. Chuang, F.-S. Kitaura et al., *The clustering of galaxies in the SDSS-III Baryon Oscillation Spectroscopic Survey: RSD measurement from the power spectrum and bispectrum of the DR12 BOSS galaxies*, *MNRAS* **465** (2017) 1757 [1606.00439].
- [78] T.M.C. Abbott, F.B. Abdalla, A. Alarcon, J. Aleksić, S. Allam, S. Allen et al., *Dark Energy Survey year 1 results: Cosmological constraints from galaxy clustering and weak lensing*, *Phys. Rev. D* **98** (2018) 043526 [1708.01530].
- [79] E. Aver, K.A. Olive and E.D. Skillman, *The effects of He I λ 10830 on helium abundance determinations*, *JCAP* **07** (2015) 011 [1503.08146].
- [80] H. Gil-Marín, J.E. Bautista, R. Paviot, M. Vargas-Magaña, S. de la Torre, S. Fromenteau et al., *The Completed SDSS-IV extended Baryon Oscillation Spectroscopic Survey: measurement of the BAO and growth rate of structure of the luminous red galaxy sample from the anisotropic power spectrum between redshifts 0.6 and 1.0*, *MNRAS* **498** (2020) 2492 [2007.08994].
- [81] P. McDonald and A. Roy, *Clustering of dark matter tracers: generalizing bias for the coming era of precision LSS*, *Journal of Cosmology and Astroparticle Physics* **2009** (2009) 020 [0902.0991].
- [82] S. Saito, T. Baldauf, Z. Vlah, U. Seljak, T. Okumura and P. McDonald, *Understanding higher-order nonlocal halo bias at large scales by combining the power spectrum with the bispectrum*, *Phys. Rev.* **D90** (2014) 123522 [1405.1447].
- [83] A. Taruya, T. Nishimichi and S. Saito, *Baryon Acoustic Oscillations in 2D: Modeling Redshift-space Power Spectrum from Perturbation Theory*, *Phys. Rev.* **D82** (2010) 063522 [1006.0699].
- [84] T.L. Smith, V. Poulin and M.A. Amin, *Oscillating scalar fields and the Hubble tension: A resolution with novel signatures*, *Phys. Rev. D* **101** (2020) 063523 [1908.06995].
- [85] V. Poulin, T.L. Smith, D. Grin, T. Karwal and M. Kamionkowski, *Cosmological implications of ultralight axionlike fields*, *Phys. Rev. D* **98** (2018) 083525 [1806.10608].
- [86] V. Poulin, T.L. Smith, T. Karwal and M. Kamionkowski, *Early Dark Energy can Resolve the Hubble Tension*, *Phys. Rev. Lett.* **122** (2019) 221301 [1811.04083].
- [87] T. Simon, P. Zhang, V. Poulin and T.L. Smith, *Updated constraints from the effective field theory analysis of BOSS power spectrum on Early Dark Energy*, **2208.05930**.
- [88] L. Herold and E.G.M. Ferreira, *Resolving the Hubble tension with Early Dark Energy*, *arXiv e-prints* (2022) arXiv:2210.16296 [2210.16296].